



Stockholm
University

Bachelor Thesis

Degree Project in
Geology 15 hp

**A sedimentological study of the occurrence of
ikaite and possible anhydrite pseudomorphs
in Neoproterozoic stromatolitic dolostones
on Islay, Scotland**

Bodil Häggström



Stockholm 2017

Department of Geological Sciences
Stockholm University
SE-106 91 Stockholm
Sweden

Abstract

The aim of this study is to document the occurrence and proximity of possible ikaite- and anhydrite pseudomorphs in outcrops of the Bonahaven Dolomite Formation along a coastal section on North Islay, Scotland. The goals were to make a stratigraphic profile to set bounds on the occurrence of the different pseudomorphs and to make a paleoclimatic/ environmental interpretation based on their stratigraphic distribution and to describe the different pseudomorphs in thin section. Scanning electron microscope and microprobe analysis of inclusions in quartz and pyrite in both the suspected ikaite pseudomorphs and suspected anhydrite pseudomorphs were confirmed as anhydrite based on the analysis results and their high birefringence and square/rectangular shapes. Similar inclusions were found in samples from all sampled units. The pseudomorph shapes also support a gypsum precursor for all pseudomorphs. A suspected microbial mat surface was sampled and confirmed as a microbial mat fossil. Preservation of sedimentary structures together with dolomite and the occurrence of gypsum in close proximity of stratabound pyrite layers is interpreted as a microbial mat mediated precipitation environment. The dolostone lithologies of the Bonahaven Dolomite formation is suggested to have been deposited in a shallow lagoon as an evaporitic and microbially mediated precipitate. Wider implications of the microbial mat environment as a possible trigger for glaciation periods in the Neoproterozoic are discussed.

Table of contents

1	Introduction.....	1
1.1	The Neoproterozoic Era.....	2
1.2	Ikaite and anhydrite pseudomorphs.....	4
1.2.1	Ikaite.....	4
1.2.2	Anhydrite and gypsum.....	6
1.3	Microbial effects on sedimentation.....	9
1.3.1	Microbially induced sedimentary structures and microfossils.....	10
1.3.2	The processes within microbial mats.....	11
2.	Geological background of the Bonahaven Dolomite Formation.....	15
3.	Methods.....	18
3.1	Field methods.....	18
3.2	Laboratory methods.....	19
3.2.1	Preparation of samples for making of thin sections.....	19
3.2.2	Scanning electronic microscope.....	19
3.2.3	Thin section visual analysis.....	19
3.2.4	Handheld X-ray fluorescence analysis.....	19
3.2.5	Microprobe analysis.....	21
4.	Results.....	22
4.1	Stratigraphic profile.....	22
4.2	Pseudomorphs described in thin section.....	24
4.3	Possible microbial mat microfossils described in thin section.....	31
4.4	Scanning electronic microscope (SEM) results.....	33
4.5	Microprobe analysis results.....	34
4.6	Handheld XRF-results.....	36
5.	Discussion of results.....	37
5.1	Stratigraphic profile.....	37
5.2	Pseudomorphs.....	39
5.3	Sedimentary structures and microfossils.....	42
5.4	Environment interpretation.....	48
6.	Wider implications of microbial effects on sedimentation.....	50
7.	Conclusion.....	52
8.	References.....	53

1. Introduction

The aim of this study is to document the occurrence of possible ikaite- and anhydrite pseudomorphs along a ~100m coastal section on North Islay, Scotland. The goals are to make a stratigraphic profile to set bounds of the occurrence of the different pseudomorphs; to describe the different pseudomorphs in thin section and to make a paleoclimatic/environmental interpretation of their proximity. The study area is located within the Bonahaven Dolomite Formation (BDF) which is a sedimentary rock formation that was deposited in the latter half of the Neoproterozoic Era. Information about the Neoproterozoic Era is provided in section 1.1 to set the background to the paleoclimatic/environmental interpretation.

A layer containing faintly pink nodule-like shapes outcrops at a wave-polished part of the north shore of Islay; western Scotland. The nodule-like shapes that occur in seemingly deformed mounds and the surrounding grey matrix resemble chicken-wire structure in appearance. This is a sedimentary structure found in evaporites where gypsum crystals have been dehydrated to form anhydrite (Ehlers & Blatt, 1982) and where anhydrite or gypsum have grown within the sediment in upper intertidal and supratidal areas of sabkhas (Warren, 2016). Anhydrite is an evaporitic mineral associated with high temperatures (Warren, 2016). Possible ikaite pseudomorphs are present further east on the same shore (Alasdair Skelton, personal communication, December 19, 2016). Ikaite growth is limited to temperatures below 4°C and is thereby useful as an indicator of cold climate (Last et al., 2013). Further information about the two contradictive climate indicators is presented in section 1.2 to provide a background to the requirements for formation of each mineral.

Close to the nodule-like shapes are frequently occurring stromatolite mounds. Stromatolites are formed by microbial mats and display an eye-catching laminated fabric (Dupraz & Visscher, 2005). Minerals that have precipitated induced by or influenced by microbial activity are called microbialites (Dupraz et al. 2008). An introduction to microbial effects on sedimentation is presented in section 1.3. There are other structural features present in the study area that can be associated with microbial activity; including well preserved wave-ripples and pyrite laminae and suspected microbial mat fossils. Microbially induced sedimentary structures and microfossils are therefore presented in section 1.3.1 to give the reader a background of the interpretation of these structures.

In section 1.3.2 microbial mats and the processes within them are presented to provide the reader with the background of how microbial activity can promote mineral precipitation and sedimentation. The production of oxygen by cyanobacteria can also be related to climate change which make the presence of microbial communities important in an environmental/paleoclimatic interpretation.

1.1 The Neoproterozoic Era

The Neoproterozoic Era is the time interval between 1000 Ma and 542 Ma (Gaucher et al., 2009). The Neoproterozoic Era is divided in three periods called Tonian, Cryogenian and a third period referred to with different names including Neoproterozoic III, Sinian, Vendian and Ediacaran (Knoll, 2000). The Tonian period began with the last 100 Ma of the 1300-900 Ma Grenvillian Orogeny (Gaucher et al., 2009). At the end of the Grenvillian Orogeny and a supercontinent called Rodinia had formed (Li et al., 2008). At around 825 Ma a super-plume peak occurred that is associated with the start of continental rifting of Rodinia (Gaucher et al., 2009). The Cryogenian period began at 850 Ma (Knoll, 2000). The continental rifting continued eventually leading to the break-up of Rodinia (Li et al., 2008). The breakup of Rodinia and consequent opening of the Iapetus ocean is thought to have occurred between 750 Ma and 600 Ma (Li et al., 2008). During the Cryogenian there were at least two global glaciation events (Hoffman et al., 1998). Glacial deposits are found from this time on most continents (Fairchild & Kennedy, 2007). Palaeomagnetic data suggests that the ice front reached the sea-level even at low latitudes (Hoffman et al., 1998). The Sturtian glaciation event occurred at 717-660 Ma followed by a ~25 Ma non-glaciation period before the Marinoan glaciation (Rooney et al., 2015). Cap-carbonates of the Marinoan glaciation are dated to 632,3 Ma (Rooney et al., 2015) and mark the end of Cryogenian and start of Ediacaran age (Prave et al., 2009). During the Ediacaran one of the first metazoan fauna was established; multicellular organisms with function-specific bodyparts (Clarkson, 1998). A less widespread glaciation period called the Gaskiers occurred around 580 Ma (Fairchild & Kennedy, 2007).

Characteristic for Neoproterozoic glacial deposits are that they often are covered by thin (<5m) dolomites called 'cap carbonates' (Fairchild & Kennedy, 2007). Low values of $\delta^{13}\text{C}$ in both cap carbonates and underlying carbonate rocks are associated with the glaciation events (Hoffman et al., 1998). The low $\delta^{13}\text{C}$ values are interpreted as a sign of collapse of the biological productivity at the ocean surface (Hoffman et al., 1998). One attempt to explain this biological collapse suggests that the whole planet was covered by ice –the snowball-Earth hypothesis (Hoffman et al., 1998). The strong albedo of the ice would then have created a positive-feedback process; eventually leading to a complete ice-cover (Fairchild & Kennedy, 2007). If the snowball-Earth hypothesis holds, this glaciation must have ended fast to overcome the albedo-feedback effect (Hoffman et al., 1998). This is suggested to have happened by enormous amounts of CO_2 released from volcanic subaerial eruptions (Hoffman et al., 1998). The CO_2 mixing in the ocean would according to the snowball-Earth hypothesis be the reason for the typical cap-carbonates (Hoffman et al., 1998). There are other suggested explanations for low-latitude glaciation than the snowball-Earth hypothesis. The high tilt-Earth hypothesis suggests a tilt of the Earth promoting glaciation close to the equator rather than the poles and the zipper-rift Earth hypothesis where regional glaciations are connected to continental rifting and the 'slush-ball Earth'-hypothesis suggests that the open ocean remained ice-free at low latitudes while the continents were glaciated to sea-level (Fairchild & Kennedy, 2007). Another explanation involves the anaerobic degradation of organic matter as a trigger for glaciation periods but without a complete ice-cover of the Earth (Tziperman et al., 2011)

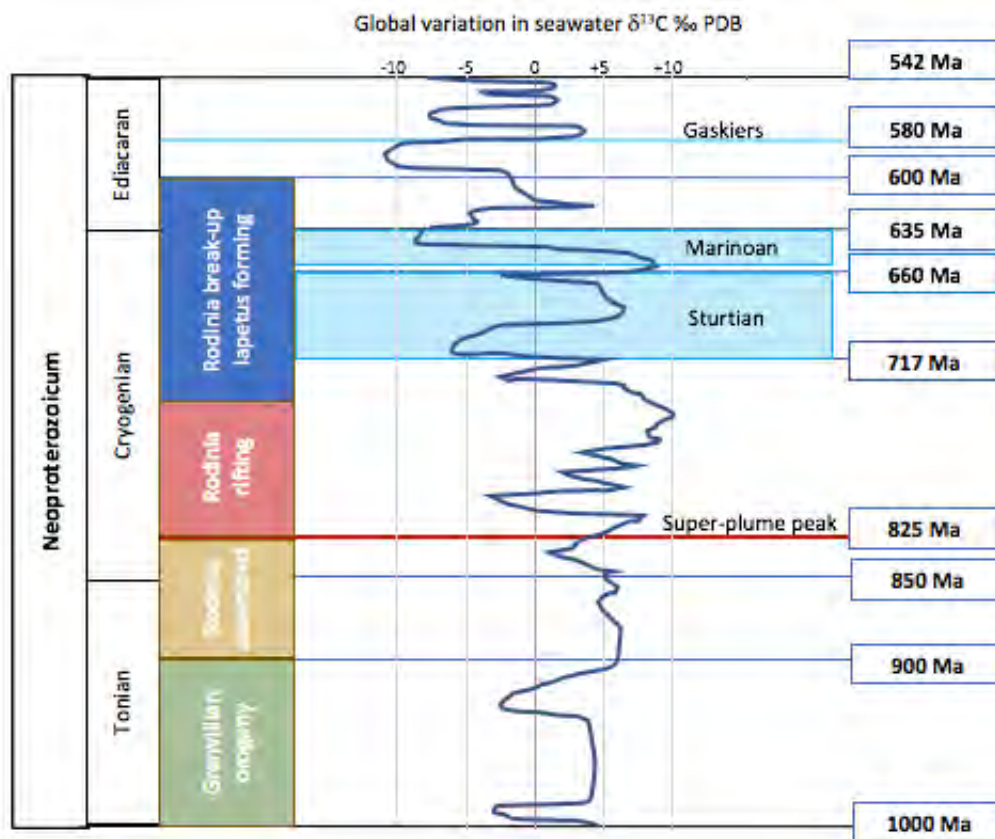


Figure 1. Timescale illustration for the Neoproterozoic Era based on the events mentioned and referenced in the text in section 1.1. Variation of $\delta^{13}\text{C}$ in carbonates curve is traced from illustration by Gaucher et al. (2009) and is re-scaled to fit the scale in this illustration.

The reason why low $\delta^{13}\text{C}$ could indicate absence of life is the fractionation that occurs during the uptake of carbon by living organisms (Brady et al., 2010). Photosynthesizing organisms incorporate the lighter ^{12}C from the CO_2 they use because the uptake of the smaller isotope is faster (Brady et al., 2010). This fractionation leaves the heavier isotopes which keeps the $\delta^{13}\text{C}$ of the dissolved inorganic carbon (DIC) pool higher in productive ocean water (Brady et al., 2010). If biologic production ceases no ^{12}C is used and the $\delta^{13}\text{C}$ DIC will be lower (Brady et al., 2010). Carbonate that precipitates from the high $\delta^{13}\text{C}$ DIC will thereby have a higher $\delta^{13}\text{C}$ footprint than carbonate precipitated from low $\delta^{13}\text{C}$ DIC (Brady et al., 2010). Low $\delta^{13}\text{C}$ values could however be explained by remineralisation of organic matter in anaerobic processes conducted by microorganisms (Tziperman et al., 2011). However, the model presented by Tziperman et al. (2011) treats oxygen production by cyanobacteria as a process only occurring in the upper ocean. In this model, buoyancy would keep most dissolved organic carbon (DOC) in the oxygenated upper ocean where aerobic remineralization would consume the produced oxygen and the underlying water would be anoxic (Tziperman et al., 2011). A net carbon drawdown would then be triggered by anaerobic remineralization through sulfate reduction in the lower water column by an increase in organic matter production (Tziperman et al., 2011). However, oxygen production and anaerobic remineralization can also occur in microbial mats on a shallow ocean floor (Dupraz & Visscher, 2005).

1.2 Ikaite and anhydrite pseudomorphs

The replacement of a mineral where the original shape of that mineral is filled with other minerals are called pseudomorphs. Different minerals can have similar outlines which can make it a challenge to tell which mineral that is replaced (Warren, 2016). Pseudomorphs after ikaite and pseudomorphs after gypsum can both display a similar pointy elongate shape and twin complexes which calls for the need of other characteristics of the replacing processes to tell them apart (Warren, 2016). Figure 4 compare one of the many shapes found of pseudomorphed ikaite and a lenticular gypsum crystal. In the following sections the formation criteria and various shapes of ikaite and anhydrite will be presented to provide a background to the interpretation of the different pseudomorphs occurring in the study area.

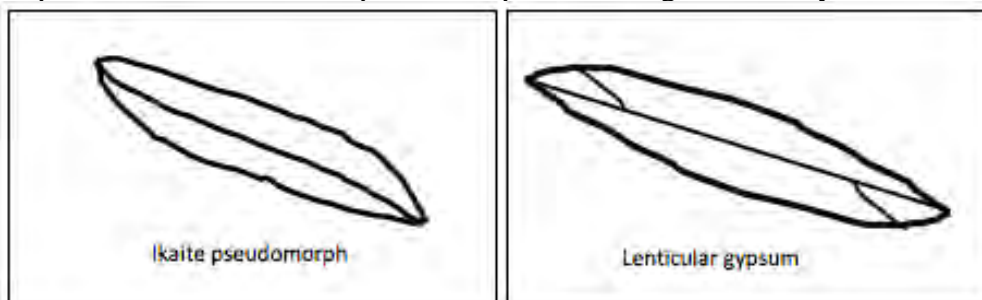


Figure 4. Illustration of the similarity of a certain ikaite pseudomorph shape to lenticular gypsum.

1.2.1 Ikaite

Ikaite ($\text{CaCO}_3 \cdot 6\text{H}_2\text{O}$) can grow in anoxic marine sediments if the temperature is close to 0°C and large amounts of HCO_3^- is provided from the decomposition of organic matter (Bischoff et al., 1993). Ikaite can also be found forming calcareous pyramid-shaped tufa-mounds or towers in cold water where Ca^{2+} is added from upwelling springs (Bischoff et al., 1993) and be formed by cryogenesis (Warren, 2016). Cryogenesis is the chemical precipitation that occurs when pure water molecules are incorporated in ice; increasing the concentration of salts in the remaining water (Warren, 2016). When subjected to warmer temperatures than 4°C ; ikaite quickly decompose to CaCO_3 and water (Bischoff et al., 1993, Last et al., 2013). Where ikaite pseudomorphs are found in the rock record they are often replaced by calcite (Last et al., 2013) Ikaite pseudomorphs have been found in a range of sizes from $<1\text{cm}$ to 1m (Hugget et al., 2005). Ikaite pseudomorph assemblages are found as Ikka-fjord-like tufas; as interpenetrating and twinned clusters on bedding surfaces or as single crystals or clusters in fine-grained organic-rich sediments (Hugget et al., 2005). If no external CaCO_3 is added during decomposition of ikaite; the remnant calcite would take up a third of the original volume (Hugget et al., 2005).

If the water is expelled away from the original space; the result is a very porous calcite pseudomorph (Hugget et al., 2005). Later infilling of micritic dolomite and calcite can occur during diagenesis (Hugget et al., 2005). The calcite can be mantled by pyrite and have a quartz rim or be completely replaced by quartz and pyrite in pseudomorphs gone through metamorphism (Dempster & Jess, 2015). Replacement by calcite of other minerals than ikaite can occur and for this reason the original shape of the mineral is important (Last et al., 2013). If the precipitation of calcite occurred simultaneously with decomposition of the ikaite the original shape can be preserved (Hugget et al., 2005).

Elongate monoclinic prisms with pyramids in both ends is a characteristic shape for non-pseudomorphed ikaite (Swainson & Hammond, 2001). The angle of the pyramid point is originally $\sim 110,5^\circ$ (Last et al., 2013, Swainson & Hammond, 2001). This makes the original ikaite distinguishable from other elongate minerals with pointy ends. The most similar angle that gypsum crystals have is for example $\sim 114^\circ$ (mindat.org). The original shape of ikaite can unfortunately be distorted during pseudomorphism by dissolution of preferred crystal faces (Swainson & Hammond, 2001). The pseudomorphs pyramidal ends in most images and illustrations displays sharper angles than the original $110,5^\circ$ (Shearman & Smith, 1985). An asymmetry where the pyramids point in opposing direction is common; tending towards a s-shape seen from the side in some pseudomorphs (Shearman & Smith, 1985, Warren, 2016). Different ikaite pseudomorph profile outlines is presented in figure 5. Pseudomorphs after ikaite have been named differently depending on the local where they are found; though glendonite is the most frequently used name (Swainson & Hammond, 2001).

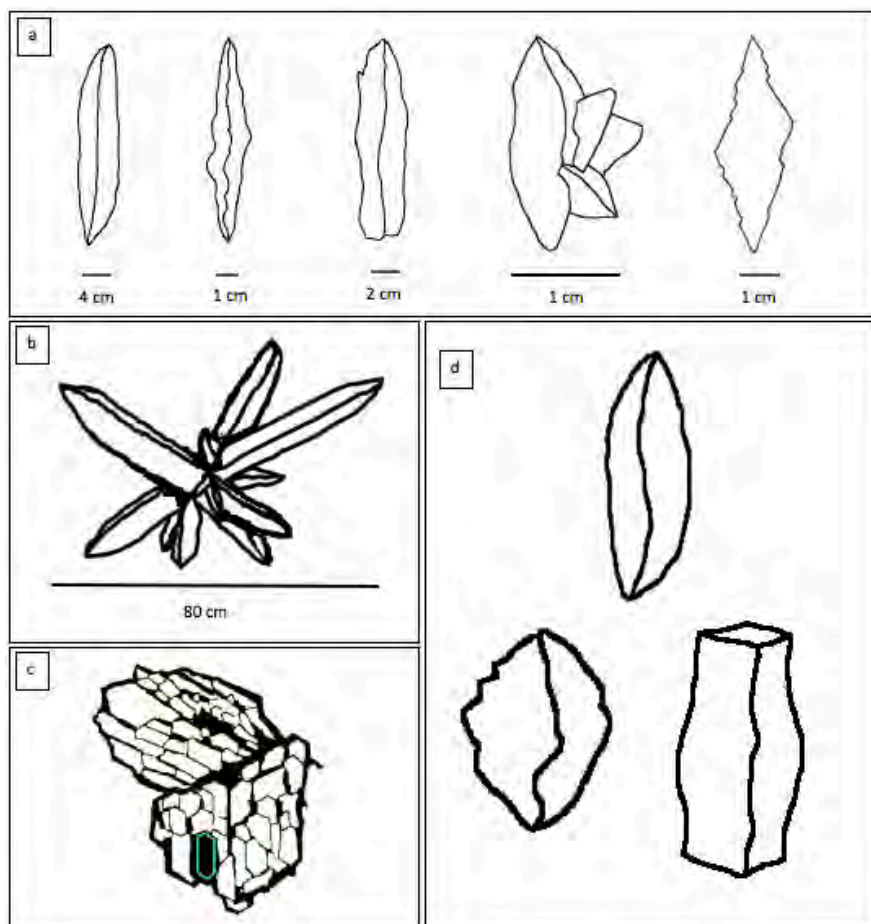


Figure 5 a) Five variants of ikaite pseudomorphs traced from illustrations in Shearman & Smith (1985). b) Ikaite pseudomorph inpenetrant cluster traced from image in Brooks (2016). c) Tracing of a SEM photomicrograph from Last et al. (2013) showing calcite pseudomorphs with preserved original shapes of ikaite. One cruystal is emphasized by a turquoise frame. (Length of grains $< 2\mu\text{m}$.) d) Three ikaite pseudomorph shapes traced from illustration in Swainson & Hammond (2001).

1.2.2 Anhydrite and gypsum

Anhydrite and gypsum are evaporitic minerals (Nichols, 2009). An evaporite is formed by a chemical process where the concentration of the participating ions is the controlling factor of mineral formation (Nichols, 2009). The base conditions for evaporites to form in a body of water is that refilling with new water is slower than the evaporation rate (Warren, 2016). When the concentrations of the participating ions of an evaporite mineral have reached saturation; the mineral can precipitate out of solution (Nichols, 2009). The first mineral that can precipitate in evaporitic conditions is the least soluble which is calcium carbonate (CaCO_3) (Nichols, 2009), at salinity levels of 36-80 g/L (Schreiber & Tabakh, 2000). Calcium sulphate saturation is reached next when the water has evaporated so that only 19% of the original seawater volume remains (Nichols, 2009). There must be enough oxygen present in the water for dissolved sulfate to reach gypsum/anhydrite saturation (Turner & Bekker, 2016).

Gypsum ($\text{CaSO}_4 \cdot 2\text{H}_2\text{O}$) is the hydrous variant of calcium sulphate (Nichols, 2009). Gypsum precipitates on the sediment surface in shallow water <10m (Schreiber & Tabakh, 2000, Nichols, 2009, Warren, 2016). Gypsum can also be formed by cryogenesis (Warren, 2016). Various crystal shapes are known for gypsum and can be affected by temperature and organic material concentration, see figure 7a (Warren, 2016). Gypsum deposits can form in a variety of shapes and sizes depending on salinity levels (Schreiber & Tabakh, 2000). In salinity levels between 80 and 140g/L gypsum and carbonate can co-precipitate and form laminae with carbonate mud and fine gypsum and/or organic material (Schreiber & Tabakh, 2000). In salinities of 140-250 g/L, gypsum crust forms that can be porous; and around 250g/L gypsum arenites that may be wave-rippled can form (Schreiber & Tabakh, 2000). At salinity levels 250-300g/L large selenitic crystals can form (Schreiber & Tabakh, 2000). The selenitic crystals are commonly vertically oriented and can form layers with a thickness of a few mm to several meters, see figure 7c (Allwood et al., 2013). Radial forms or domes are common features of selenitic gypsum (Allwood et al., 2013). In a basin where the whole water column has a uniform temperature and chemistry due to throughout circulation; twinned so called “swallow-tail gypsum” crystals of cm-dm size can grow (Warren, 2016). The swallow-tails are though rare; the more common shape of large selenitic crystals have curved faces ending in a hook-like shape sometimes called “bird-beak gypsum” (Warren, 2016). See figure 7b for the different shapes. Elongate skeleton-like crystals up to ca15 cm, sabre-like crystals up to 90 cm and giant columnar or randomly oriented selenitic intergrowth crystals up to 3,5 m are other reported gypsum shapes (Kasprzyk, 2003). When less saline water mixes in to the water where gypsum grows; the crystals can start to dissolve which can truncate the tips of swallow-tail twins (Abrantes et al., 2016).

Calcium bound to the EPS in microbial mats can act as gypsum crystal nucleation sites (Allwood et al., 2013). It is therefore not unusual that layers of vertical gypsum crystals grow on top of microbial mats (Allwood et al., 2013). Gypsum lets light through so that the cyanobacteria can continue to produce oxygen (Warren, 2016). Microbial mats can also grow on top of selenitic gypsum and when the crystals grow the mat gets included in the crystal, leaving a microbial lamination in the gypsum (Allwood et al, 2013).

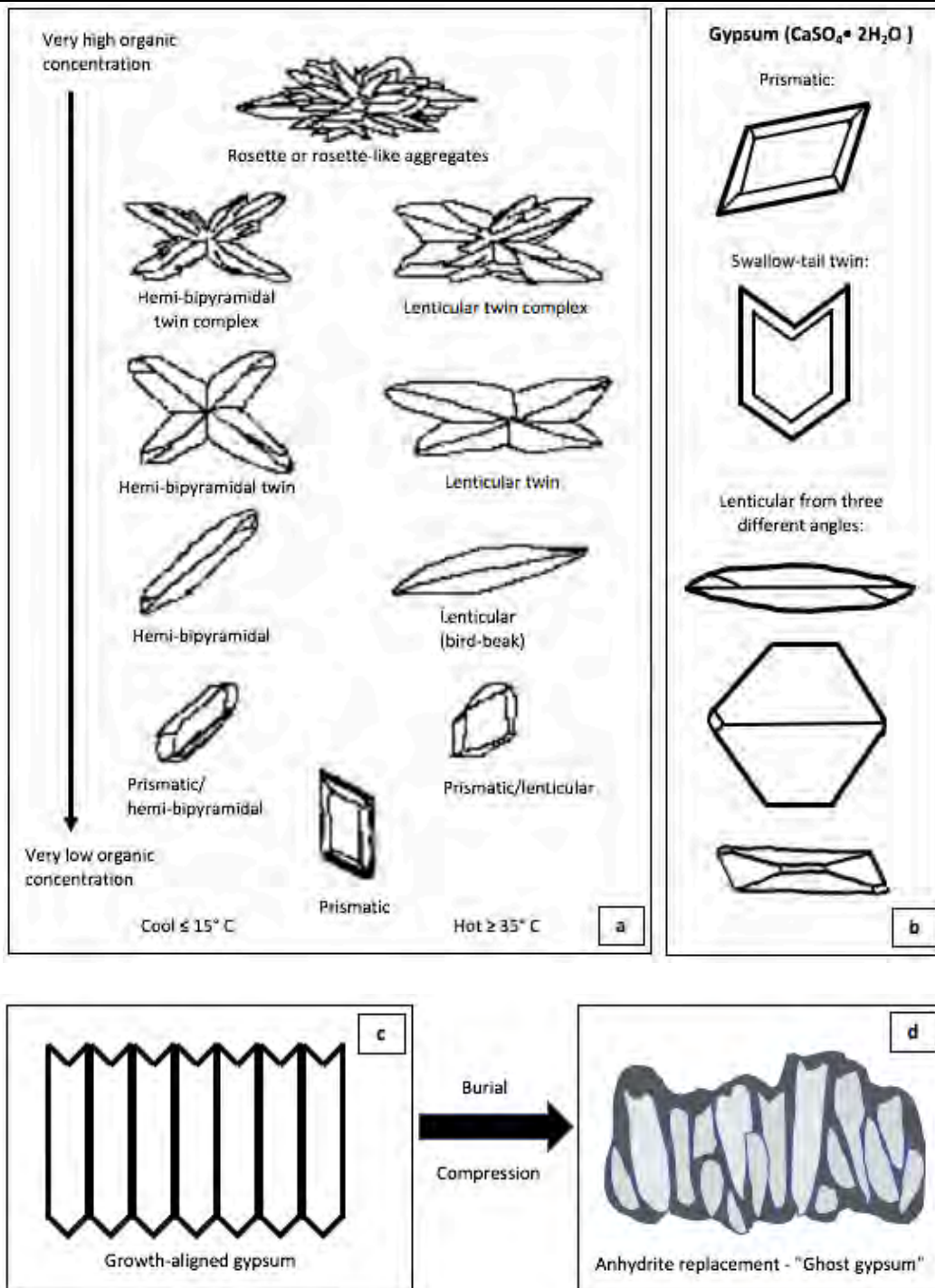


Figure 6 **a)** Gypsum crystal habits depending on organic concentration and temperature from laboratory experiment by Cody & Cody 1988 (Warren, 2016). **b)** Prismatic gypsum crystal, swallow-tail twin gypsum crystal, lenticular gypsum crystal seen from three different angles (Warren, 2016). **c)** Vertical growth of bottom-nucleated selenitic gypsum. Even though swallow-tail is not extremely common, it is often used to illustrate gypsum (Warren, 2016). **d)** Replacement of gypsum by anhydrite during burial and compression leaves “ghost gypsum” (Warren, 2016).

Sulphate reducers can dissolve available calcium sulphate when SO_4^{2-} becomes depleted in pore-waters during early burial (Warren, 2016). If amorphous silica is available; local variations of pH can cause re-precipitation of microcrystalline quartz which replaces the dissolved calcium sulphate along the edges of the crystals (Warren, 2016). The microcrystalline quartz mimics the outline of the crystal (Warren, 2016). The texture of a replaced crystal or nodule depends on the rate of sulphate reduction and the amount of available dissolved silica (Warren, 2016). Synchronized dissolution and replacement can leave calcium sulphate inclusions (Warren, 2016). The consumption of sulfate from calcium sulphate leaves Ca^{2+} available for subsequent sparry carbonate precipitation (Warren, 2016). The alteration of calcium sulphate to carbonate is called evaporite calcitization (Warren, 2016). Sulphate reduction can also occur abiotically during deep burial; however the most reported setting for evaporite calcitization is during early diagenesis (Warren, 2016). Calcium sulphate that is not decomposed by bacteria can be dissolved by metamorphic fluids and leave an open vug where dissolved silica can precipitate as coarse quartz grains (Warren, 2016). Barite, metal sulphides and sparry carbonate can fill the remaining space in the middle in later diagenetic stages if quartz have not filled the entire space (Warren, 2016).

Barite (BaSO_4) is a very common replacement mineral of both gypsum and anhydrite (Warren, 2016). Barite can replace gypsum and anhydrite during early diagenesis when the ratio of activity $\text{Ca}^{2+}/\text{activity Ba}^{2+}$ is less than $10^{5.5}$ (Warren, 2016). The replacement take place through the reaction $\text{CaSO}_4 + \text{Ba}^{2+} \leftrightarrow \text{BaSO}_4 + \text{Ca}^{2+}$ (Warren, 2016). The higher the temperature gets; the more likely barite replacement of anhydrite will take place due to the higher solubility of anhydrite with increasing temperature (Warren, 2016). Barite is also common as replacement or filling in any geologic environment where barium-rich and sulphate-rich fluids have the possibility to mix; such as cold seeps and hydrothermal vents (Warren, 2016). For barite precipitation close to the surface; microbes are suspected to be important (Warren, 2016). Isotope trends in $\delta^{34}\text{S}$ compared to $\delta^{18}\text{O}$ in barite from the Gulf of Mexico indicates that the barite is formed from seawater sulphate that is altered by microbial sulphate reduction (Warren, 2016).

Anhydrite (CaSO_4) is the anhydrous variety of calcium sulphate (Nichols, 2009). Anhydrite can precipitate within the sediment at the shorelines in arid environment (Nichols, 2009, Schreiber & Tabakh, 2000). Anhydrite can be hydrated into gypsum in contact with water (Nichols, 2009) and gypsum can be dehydrated into anhydrite during burial (Schreiber & Tabakh, 2000, Nichols, 2009). Gypsum dehydrates to anhydrite when the surrounding temperature gets 50-60°C; temperatures that can be reached within a few meters to >1km deep burial (Warren, 2016). At near-halite saturation, the dehydration can already happen at 35-40°C (Warren, 2016). A 40% water-filled porosity is created during dehydration (Warren, 2016). The released water can cause deformation of the bed (Warren, 2016). Replacement of selenitic gypsum by anhydrite during burial can preserve the shape outline of the original gypsum; resulting in elongate “ghost-gypsum” anhydrite nodules (Warren, 2016). Replacement of gypsum by anhydrite on burial can leave residues of the original gypsum in the product anhydrite nodules and vice versa (Warren, 2016). The shape of anhydrite crystals is presented in figure 7b. Nodular forms of both anhydrite and gypsum can grow within the sediment in upper intertidal and supratidal areas of sabkhas due to capillary evaporation of pore waters (Warren, 2016). These rounded nodules form an entherolitic or chicken-wire structure, see figure 7a (Warren, 2016). Nodules push the sediment aside as they grow (Warren, 2016).

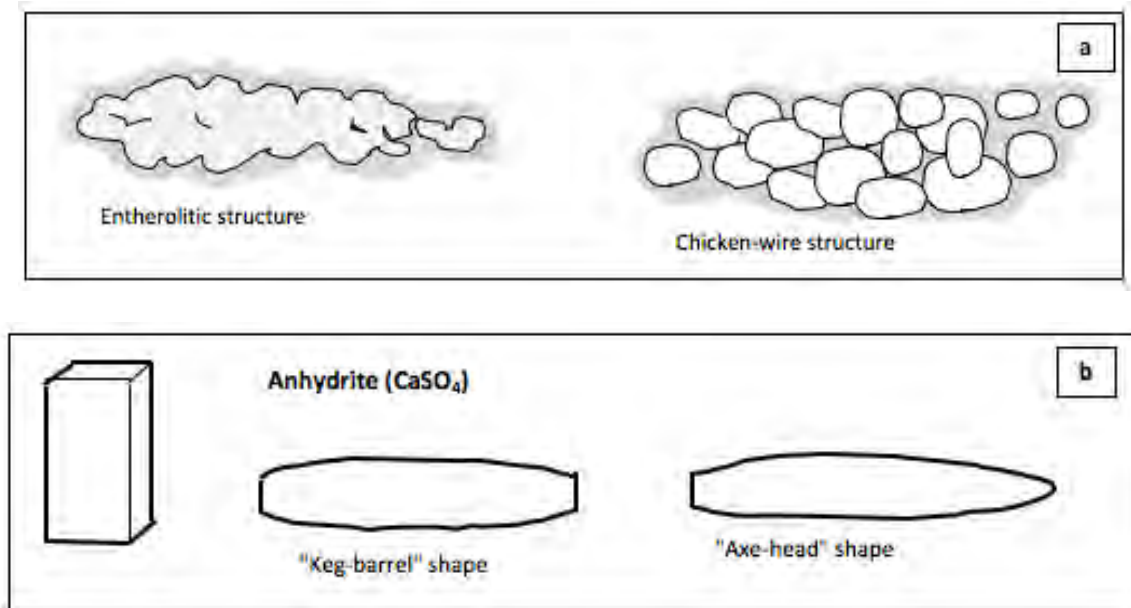


Figure 7 a). Entherolithic and chicken-wire nodular growth of anhydrite and gypsum in sabhka sediment (Warren, 2016). **b)** Anhydrite crystal shape, "axe-head" and "beer-keg" lenticular anhydrite (Warren, 2016).

1.3 Microbial effects on sedimentation

Microbial mat communities were the dominant life-form on our planet through almost 85% of Earth's history (Dupraz et al. 2008). Microbial mats can both passively trap and actively precipitate sediment (Dupraz & Visscher, 2005). Stromatolites that were commonly forming in the Precambrian shallow oceans (Dupraz & Visscher, 2005) are laminated structures formed by microbial mat communities (Dupraz et al. 2008). Stromatolites can display domed, columnar and conical morphologies (Allwood et al., 2013). Minerals that have precipitated induced by or influenced by microbial activity are called microbialites (Dupraz et al. 2008). Other examples of less eye-catching microbialites than stromatolites are thrombolites and leiolites (Dupraz et al. 2008). Thrombolites have a clotted macrofabric and leiolites displays no visible macrostructure at all (Dupraz et al., 2008). Lamination can be absent because the chemical compounds diffuse from their original position during diagenesis due to decomposition by the microbes (Noffke et al., 2013). The precipitation influenced by the chemical compounds released in microbial mats react with the chemical compounds of the surrounding water and result in initially hydrated minerals which dehydrate; shrink and recrystallize during diagenesis (Noffke et al., 2013). The resulting mineral clots are shaped by the original pattern of the organic lamination within the mat (Noffke et al., 2013).

At the end of the Precambrian more advanced lifeforms evolved that grazed on the mats and stromatolite formation became less common (Dupraz et al, 2008). The settings where modern microbial mats are found include environments where water is present at least periodically such as ocean shelves and various ocean coast areas like lagoons and tidal zones, freshwater shores and lakes and interdune areas (Noffke et al., 2013). In a calm lagoon; microbial mats can pile upon each other in stacks reaching meter-scale thickness (Noffke et al., 2013).

1.3.1 Microbially induced sedimentary structures and microfossils

Microbial mats living within deposited sediment can make the sedimentary surface 3-5 times more stable and microbial mats living on top of the sediment can make the sedimentary surface 12 times more stable (Noffke et al., 2013). Microbial communities can also occur as thin biofilm overgrowths; preserving sedimentary features like wave ripples (Noffke et al., 2013). Preserved traces of microbial mats in the sediment they grew in that are not precipitation-related are called microbially induced sedimentary structures; in short 'MISS' (Noffke et al., 2013). MISS can be preserved through low grade metamorphism and is found worldwide and as far back in the geological record as 3.48 Ga (Noffke et al., 2013). Currents can wrinkle and erode flakes from the mats; leaving fringed edges (Noffke et al., 2013). When sediment covers the mat; cyanobacteria in need of sunlight for their survival can migrate upwards along filaments through the sediment perpendicular to the surface and leave filament ridges and tufts (Noffke et al., 2013). Microbial mats in upper supratidal zones that are seasonally completely dry; shrink and leave polygonal cracks (Noffke et al., 2013). The edges can be rolled up and centers of polygons can be domed upward because of rising gas produced by microorganisms in the lower part of the mat (Noffke et al., 2013). All these structures can be preserved in the sedimentary record as MISS (Noffke et al., 2013). Bamboo leaf-like, worm- and sinuous cracks, mineral grain alignment, pyrite and micrite laminae are other examples of MISS (Lan & Chen, 2012). Some of the features of modern microbial mats in the Giavola Lagoon in Greece are shown in figure 2.

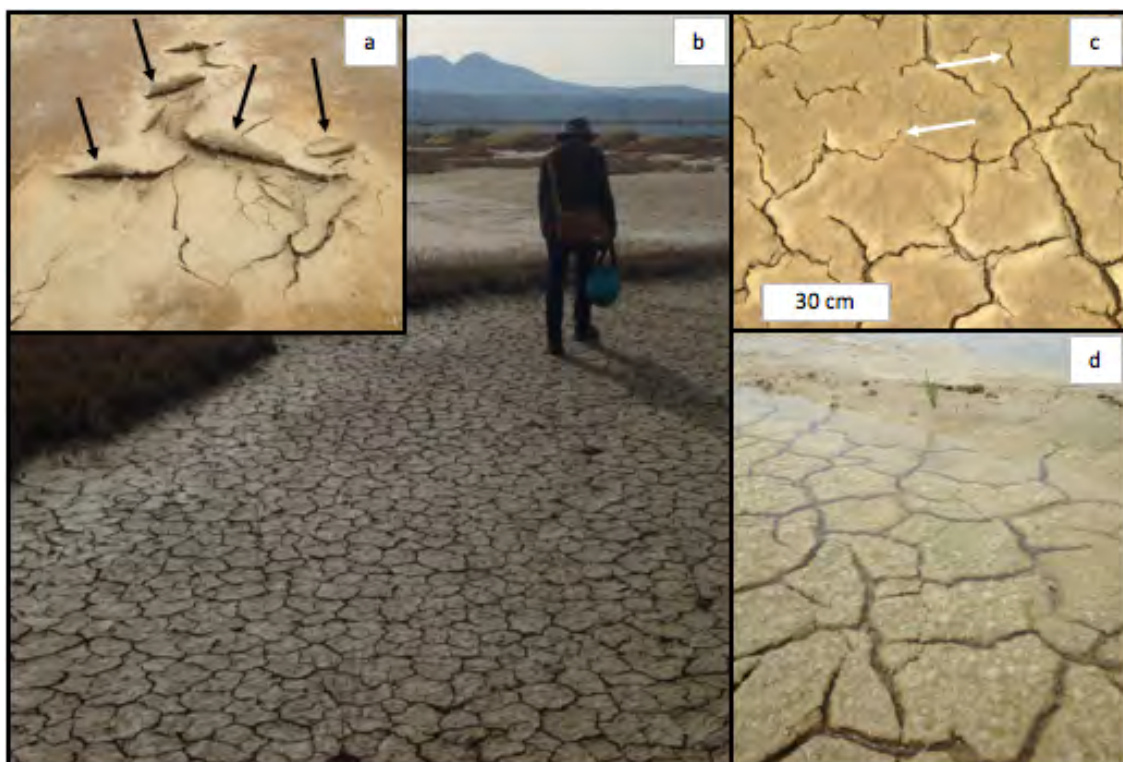


Figure 2. Microbial mats at the Giavola Lagoon in Greece. A) Rolled up edges of a drying microbial mat and the white arrow points at a microbial mat-flake. B) The surface of the dried mats is rigid enough to walk on. C) Polygonal cracks forming in drying mat. White arrows point out small sinuous cracks. C) When the mat gets covered by water the oxygen production recovers fast and the mat turns green. Bubbles indicate production of gas (which in this case probably is oxygen) that accumulates under a surface of EPS (Volker Brüchert, personal communication, April 17, 2017).

Mineralization of the organic matter can preserve the features of microbial mats during diagenesis (Noffke et al., 2013). The original organic matter is often replaced by iron sulphide (pyrite) and iron oxides (hematite and goethite) (Noffke et al., 2013). The coating or replacement of organisms by minerals where the original morphology of the organism is preserved is called fossilization (Javaux & Benzerara, 2009). Microscopic remains of organisms are called microfossils (Javaux & Benzerara, 2009). Carbonate precipitated onto cyanobacterial sheaths can preserve the organic material within and leave a carbonaceous microfossil (Javaux & Benzerara, 2009).

Microfossils can be preserved through high grade metamorphism (Javaux & Benzerara, 2009). Organic material undergoes thermal maturity by graphitisation during burial (Javaux & Benzerara, 2009). The degree of graphitisation indicates the peak pressure and temperature during burial/metamorphism and can be estimated by Raman microspectroscopy (Javaux & Benzerara, 2009).

1.3.2 The processes within microbial mats

The metabolic rate within a microbial mat is higher than other benthic ecosystems and rival the element cycling rate of rainforest per surface area (Dupraz & Visscher, 2005). The metabolism of the microbes in a microbial mat can directly induce mineral precipitation (Dupraz et al., 2008). Whether active carbonate precipitation occurs or not in microbial mats depends on the balance between the different processes in the mat (Dupraz et al., 2008). The photosynthesizing and reducing processes favour carbonate precipitation while the other processes favour carbonate dissolution (Dupraz et al., 2008). When carbonate precipitation occurs; the effect is a draw-down of CO_2 (Tziperman et al., 2011). Both carbonate, silicate and sulfate precipitation can be mediated by microbes (Dupraz & Visscher, 2005). The precipitated carbonate can be aragonite, calcite, monohydrocalcite, vaterite, high Mg-calcite to Ca-dolomite (Dupraz et al. 2008). Direct dolomite precipitation from seawater is normally inhibited by SO_4^{2-} which strongly pairs with Mg^{2+} ions but can be precipitated within microbial mats because the sulfate reducers use the available SO_4^{2-} (Wright & Wasey, 2005).

Mineral precipitation can also be passively influenced by the chemistry in microbial mats and by ions adsorbing to the extracellular polymeric substances (EPS) (Dupraz et al., 2008). EPS is an organic matrix produced by the microbes (Dupraz et al., 2008). EPS protect the cells from external disturbance and the sticky surface can trap sediment (Noffke et al., 2013). EPS have acidic groups which are negatively charged and can bind ions such as Mg^{2+} and Ca^{2+} (Dupraz et al., 2008). When the EPS is degraded; the cations are released and can bind to carbonate ions instead (Dupraz et al., 2008). Carbonate can also precipitate where all the sites for EPS ion binding are already taken (Dupraz et al., 2008). The minerals precipitating on or within a microbial mat often have rounded shapes differing from the sharp forms of inorganic precipitated minerals (Dupraz et al., 2008).

Microbial mats consist of different types of microorganisms (Dupraz et al., 2008). During calm conditions the microbes arrange themselves into layers promoting optimized interaction between the different microbe types (Noffke et al., 2013). A simplified microbial mat profile and the interaction between the different types of microbe groups is presented in figure 2.

The cyanobacteria are the primary producers on top of the microbial community and they use aerobic photosynthesis to make organic compounds (Dupraz et al., 2008). The cyanobacteria promote carbonate precipitation during the day through the net effect of carbon fixation by photosynthesis coupled with the effect of alkalinity increase: $2\text{HCO}_3^- + \text{Ca}^{2+} \rightarrow \text{CaCO}_3 + [\text{CH}_2\text{O}] + \text{O}_2$ (Dupraz et al., 2008). When photosynthesizing organisms preferably incorporate lighter ^{12}C in organic molecules the organic molecules thereby get depleted in ^{13}C (Brady et al., 2010). Organic carbon usually has $\delta^{13}\text{C}$ values between -20‰ to -25‰ PDB (Campbell, 2006). When heterotrophic organisms consume organic material; the CO_2 and HCO_3^- that gets produced will inherit the $\delta^{13}\text{C}$ value from the organic material because almost no fractionation occurs in this process (Brady et al., 2010, Campbell, 2006). The low $\delta^{13}\text{C}$ will add to the DIC-pool and affect the $\delta^{13}\text{C}$ value of carbonates precipitated (Brady et al., 2010).

Aerobic heterotrophs use organic carbon as an energy source and needs oxygen. For this reason they must live in the topmost layer too where both oxygen and organic carbon are available (Dupraz et al., 2008). Anoxygenic phototrophs need light but not oxygen and can thereby live below the oxygenated level (Dupraz et al., 2008).

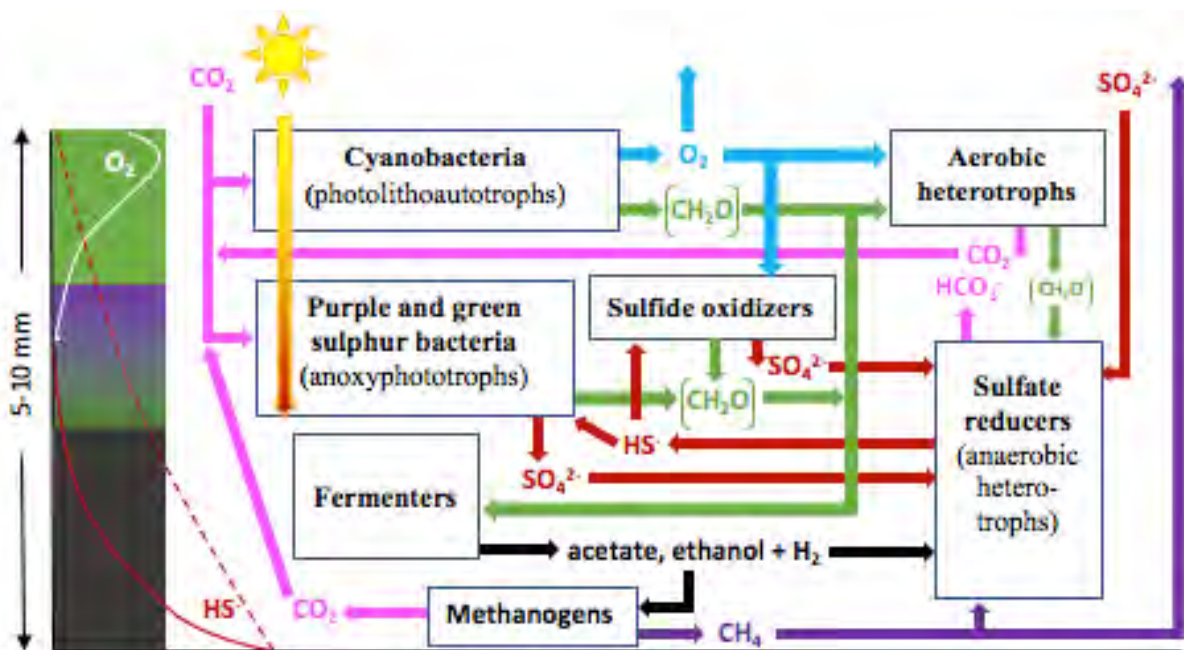


Figure 2. Simplified metabolic flow-scheme and vertical profile of a microbial mat. During the night when there is no oxygen production the sulfate reducing (HS^- producing) process begins higher up, marked by the dashed red line. The large CH_2O -notation refers to complex organic molecules and the smaller refers to simpler organic molecules like alcohols and fatty acids. The figure is based on figures and information in Dupraz et al. (2008) and Warren (2016).

Key for organism-describing words: (*photo-*) = Photosynthesizing, (*-litho-*) = dependent on inorganic compounds, (*-autotrophs*) = making their own organic carbon, (*aerobic*) = dependent on oxygen, (*heterotrophs*) = feeding on organic carbon made by other organisms, (*anoxyphototrophs*) = photosynthesizing with other oxidizing compound than oxygen (Warren, 2016).

Sulfate reducing bacteria are anaerobic heterotrophs that uses sulfate (SO_4^{2-}) instead of oxygen and can live below the oxygenated level (Dupraz et al., 2008). Sulfate reducers are independent of light and the process can proceed both day and night (Dupraz et al., 2008). Carbonate precipitation is favoured by sulfate reducers through the coupled reaction: $\text{Ca}^{2+} + \text{OH}^- + \text{SO}_4^{2-} + 2[\text{CH}_2\text{O}] \rightarrow \text{CaCO}_3 + \text{CO}_2 + \text{HS}^- + 2\text{H}_2\text{O}$ (Dupraz et al., 2008).

There are anaerobic heterotrophs that use other compounds than sulfate to oxidize organic material (Campbell, 2006). One example is the iron reducers (Campbell, 2006). The iron reducers use components with Fe^{3+} to Fe^{2+} by the either of the reaction: $2\text{CH}_2\text{O} + 8\text{Fe}(\text{OH})_3 \rightarrow 8\text{Fe}^{2+} + 2\text{HCO}_3^- + 14\text{OH}^- + 6\text{H}_2\text{O}$ (Tziperman et al., 2011). The high increase in alkalinity from the iron reducing process promotes carbonate precipitation (Tziperman et al., 2011). The HS^- produced by sulfate reduction can bind to Fe^{2+} to form pyrite (FeS_2) by the reaction $\text{Fe}^{2+} + 2\text{HS}^- \rightarrow \text{FeS}_2 + 2\text{H}^+$ (Tziperman et al., 2011).

Fermenters are organisms that break down organic material where oxygen is not available (Dupraz et al. 2008). Sulfate reducers and methanogens compete for the products of fermenters, why methanogens are confined to the lowest area in the mat where all sulfate is depleted (Campbell, 2006). Methanogens use products from fermenters (ethanol, acetate) to produce methane in two steps: $\text{CH}_3\text{OOH} \rightarrow \text{CO}_2 + \text{CH}_4$ and $\text{CO}_2 + \text{H}_2 \rightarrow \text{CH}_4 + \text{H}_2\text{O}$ (Campbell, 2006).

2 Geological background of the Bonahaven Dolomite Formation

The Bonahaven Dolomite Formation (BDF) is a stratigraphic unit within the Dalradian Supergroup (Prave et al., 2009). The sediments of the Dalradian Supergroup were deposited unconformably on top of the 1800 Ma Rhinns complex at the edge of the Laurentian continent during the breakup of Rodinia and consequent opening of the Iapetus (Webster et al., 2015). There are no fossils which can be used to determine the age of the Dalradian deposits; but it is thought to have been deposited between ca 750 and 600 Ma (Webster et al., 2015). The Islay succession of the Dalradian Supergroup consists of three groups; the Grampian, Appin and Argyll groups (Webster et al., 2015).

The Grampian group has two formations, the Colonsay group with deltaic and submarine fan deposits and the Bowmore sandstone deposited in shallow sea (Webster et al., 2015). According to possible map reconstructions of the supercontinent Rodinia's position between 750 Ma and 600 Ma (Li et al., 2008); the first of the Dalradian sediments got deposited at a latitude between the equator and 30°S. The Appin group from oldest to youngest are Maol an Fhithich Quartzite, Glen Egedale Slate, Kintra Dolostone, Mullach Dubh Phyllite to Mulindry Bridge Slate, Ballygrant and Lossit Limestone (Webster et al., 2015). The Ballygrant and Lossit limestone are separated by a metamudstone unit (Webster et al., 2015).

The Argyll group begins with the Port Askaig Formation; an inferred glacial deposit interpreted to be from the global Sturtian glaciation event (Prave et al., 2009). Studies of the Port Askaig Formation stratigraphy have revealed that the diamictite units within the earlier stages are mainly influenced by tectonic activity with only occasional glacial-influenced deposits (Arnaud & Eyles, 2006). The tectonic activity during the development of the Dalradian Basin is interpreted to have caused gravity driven sediment flows represented by diamictites and conglomerates followed by turbiditic mudstones and sandstones reworked by tidal currents (Arnaud & Eyles, 2006). Later stages of the Port Askaig Formation show more evidence of sea-ice deposition; though interlayered with current-dominated depositions which suggests a fluctuating ice margin (Arnaud & Eyles, 2006). Diamictites are completely missing from the uppermost 200-500 m of the Port Askaig Formation (Skelton et al., 2015).

The Bonahaven Dolomite Formation overlies the Port Askaig Formation (Webster et al., 2015). The succession of strata between the carbonate-containing BDF units and the diamictites of the Port Askaig Formation suggests that the BDF is probably not a *sensu stricto* cap-carbonate (Prave et al., 2009, Webster et al., 2015).

The Argyll Group units overlying the BDF are the Jura Quartzite (deposited in a tidal gulf), the Jura slate and Scarba Conglomerate (deposited in deeper water), the Port Ellen Phyllite and Ardmore Grit and Laphroaig Quartzite (deposited in the opening Iapetus ocean basin).

With Laurentia moving southwards; the last Dalradian sediments got deposited at a latitude close to 60°S (Li et al., 2008). There is however at least one alternative suggestion that the south coast of Laurentia was still close to 30°S by 600 Ma (Li et al., 2008).

Between 460 Ma and 480 Ma the Grampian orogenic event that took place (Prave et al., 2009). During the orogeny; the stack of strata got folded and the Islay anticline formed (Webster et al., 2015). Later erosion now reveals outcrops of the different units (Fig 8; Webster et al., 2015; Skelton et al., 2015). Despite the BDF being affected by greenschist facies metamorphism during the Grampian orogeny; many original features from deposition of the stratigraphic units are well preserved (Prave et al., 2009).

Maximum pressure during metamorphism was 1.0 ± 0.2 GPa and maximum temperatures were 410-470°C (Skelton et al., 2015). The Islay Anticline worked as a pathway for large volumes of buoyant metamorphic fluids (Skelton et al., 2015).

In the Lossit Limestone Formation, there are unusual low values of $\delta^{13}\text{C}$. This $\delta^{13}\text{C}$ anomaly is named the Islay anomaly (Skelton et al., 2015). The alteration by metamorphic fluids is found to be partially responsible for the Islay anomaly (Skelton et al., 2015). Carbonate rock samples from the Lossit Limestone and quartz/carbonate veins show a decreased values of $\delta^{18}\text{O}$ and $\delta^{13}\text{C}$ closer to the anticline axis (Skelton et al., 2015). Alteration by metamorphic fluid flow is less the Bonahaven Dolomite. Here, $\delta^{18}\text{O}$ values decrease while $\delta^{13}\text{C}$ increase away from the anticline (Skelton et al., 2015). The $\delta^{13}\text{C}$ (V-PDB) values in BDF vary between -3.62‰ and -8.39 ‰ with an increasing trend of higher values upwards in the stratigraphy (Prave et al., 2009). The $\delta^{13}\text{C}$ (V-PDB) values presented by Skelton et al. (2015) vary between -7,6‰ and +10.0‰.

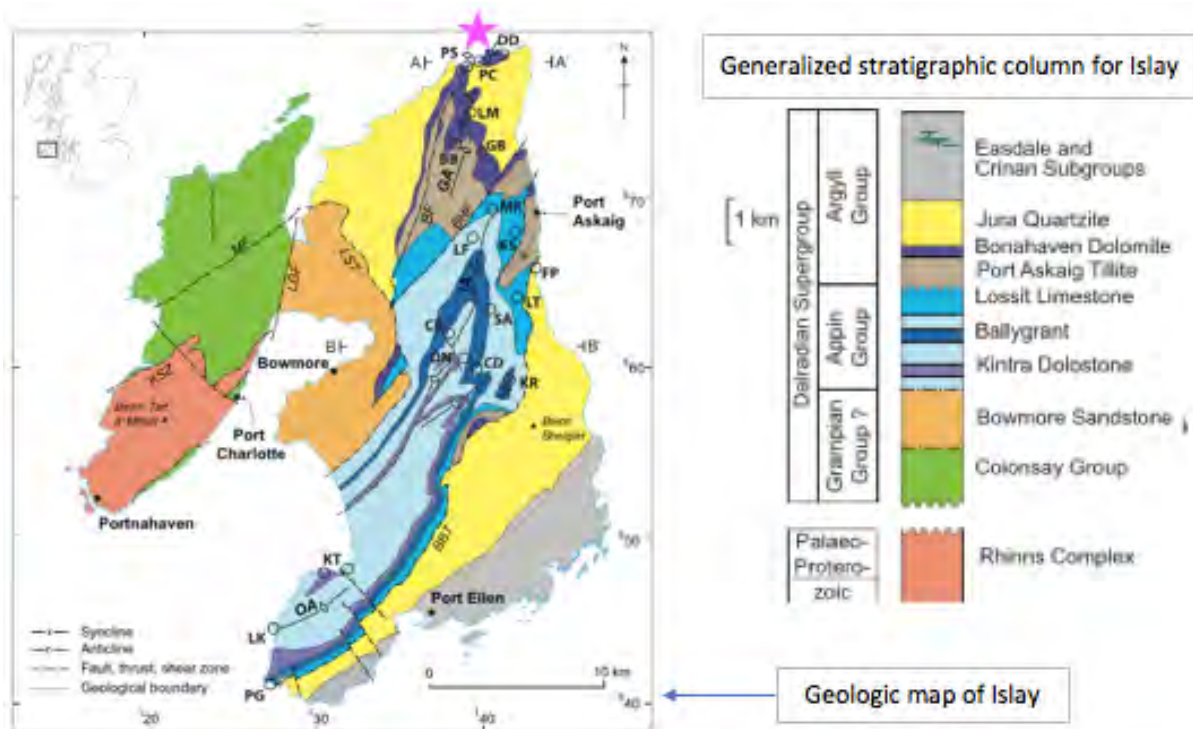


Figure 8. Geological map of Islay and a generalized stratigraphic column of the rocks of Islay from Skelton et al. (2015). The pink star marks out the study area at Port an t-Struthain, North Islay.

The Bonahaven Dolomite Formation is divided into four members (Fairchild, 1980a). Member 1 comprises five units which are of different thickness in different sections at Caol Ila and Bonahaven (Fairchild, 1991a). Unit 1 comprise 0-8 m mudrocks with lenticular bedding deposited off-shore and shallowing upwards into unit 2 which comprise 0-18m flaser-bedded sandstones with alternating horizontal and wave-ripple laminations (Fairchild, 1991a). The base of the 0-11 m thick unit 3 contains clasts of mudstone, dolostone and granite overlain by sandstones with horizontal bedding and crossbedding and possibly comprise a tidal channel-fill inlet (Fairchild, 1991a). Unit 4 comprise 0-15m sand/silt/mudstones and is interpreted as a lagoonal deposit with back-barrier washover sands (Fairchild, 1991a). There is lenticular bedding in the bottom part of unit 4 followed by wave-ripple and horizontal lamination and low angle crossbedding (Fairchild, 1991a). The topmost part of unit 4 has desiccation cracks, mudstone clasts and wave-ripple lamination (Fairchild, 1991a). Unit 5 is interpreted as a back-barrier tidal sand flat/mudflat and comprise 0-10m dolostones with some mudstone and dolostone clasts, horizontal lamination, crossbedding and climbing ripples (Fairchild, 1991a).

Member 2 consists of 22-30m quartzite with horizontal lamination and crossbedding in the bottom layers which possibly is a beach deposit and with horizontal- and wave-ripple lamination above and is possibly a subtidal-tidal shelf deposit (Fairchild, 1991a).

Member 3 contains three different facies (Fairchild, 1980a). The three facies are stromatolite-, sandstone- and layered facies (Fairchild, 1980a). The stromatolites occur as single mounds, bioherms, and in thick layers as biostromes (Fairchild, 1980a). The bioherms are incorporated in the layered facies and the biostromes are found within the sandstone facies (Fairchild, 1980a). The sandstone facies contains cross-bedding and alternates with layers of pure dolostone or dolostone pebbles (Fairchild, 1980a). Between the sand layers there are thick layers of very fine-grained dolostone; indicating a calm period between the sand depositions which are interpreted as rare storm-events (Fairchild, 1980a). The layered facies display cm-bedded dolomitic sandstone and silty dolomicrites where terrigenous clay is commonly interbedded (Fairchild 1980a). There are three subfacies of the layered facies (Fairchild 1991b). A rippled subfacies displays thick sandy storm-layers with wave-rippled laminations and finer carbonaceous layers with abundant shrinkage cracks (Fairchild, 1991b). A lenticular-graded subfacies display thin lenticular/graded sandy storm-layers where shrinkage cracks are sometimes present (Fairchild, 1991b). A scoured dolostone subfacies has irregular horizons that are modified by desiccation and clay-flakes are often accumulated in dessication cracks (Faithchild, 1991b). The involvement of microbacteria is thought to have played a role in the dolomitization (Fairchild, 1980a).

Member 4 comprise pure dolostone interpreted as a supratidal flat in the middle with fine sand and slate below and above (Fairchild, 1991b). Mudstones in the topmost part are interbedded with the overlying Jura Quartzite (Fairchild, 1991b).

3 Methods

3.1 Field methods

A stratigraphic profile was made of a sequence of the Bonahaven Dolomite Formation along the northern shore of Islay. Occurrence of pseudomorphs, stromatolites and other possible microbial mat related features was documented along the profile. The profile began at a fault represented by a breccia outcrop on the shore (N 55°55.534', W 006°10.611'). The stratigraphic profile was positioned along outcrops of fold limbs dipping in a westerly direction to ensure that the profile was from oldest to youngest strata. The younging direction is evident by stromatolites which dome upward; crack filling features and erosion surfaces with clasts from the lower layer incorporated in the layer above.

Eleven samples were collected in the study area. One sample was collected from the Lossit Limestone Formation for comparative purposes. On every sample dip and strike was measured and marked on one surface for orientation.

Sample ID/ Orientation	Location (WGS84)	Description
17-BH-PAS-01 130/78	N 55°55.544', W 006°10.659'	Possible ikaite pseudomorphs in dolo-sand fills, 2 nd meta-mudstone sequence in section A
17-BH-PAS-02 257/52	N 55°55.552', W 006°10.739'	Finely laminated siliclastic dolostone, quartzite-like, very fine pyrite laminae, suspected thin fluorite vein
17-BH-PAS-03 151/52	N 55°55.544', W 006°10.659'	Meta-mudstone beddingplane, fine dolo-sand in elongated shapes
17-BH-PAS-04 204/74	N 55°55.538', W 006°10.941'	Possible anhydrite pseudomorph 3 rd layer in second sequence in section C
17-BH-PAS-05 342/60	N 55°55.515', W 006°11.069'	Possible microbially induced sedimentary structure, "tufty" mat
17-BH-PAS-06 190/60	N 55°55.543', W 006°10.900' *	Second possible anhydrite pseudomorph layer in first sequence
17-BH-PAS-07 190/63	N 55°55.543', W 006°10.878'	Anticline hinge conglomerate, first possible anhydrite pseudomorph layer in first sequence
17-BH-PAS-08 072/84	N 55°55.533', W 006°10.635'	Possible ikaite pseudomorphs in grey dolostone with pyrite laminae
17-BH-PAS-09 141/43	N 55°55.552', W 006°10.985'	Last occurrence of possible anhydrite pseudomorph, 1 st or 2 nd sequence
17-BH-PAS-10 158/88	N 55°55.551', W 006°11.001'	Vein at wall with stromatolite mound, western end of stratigraphic profile section
17-BH-PAS-11 133/59	N 55°55.544', W 006°10.991'	Vein with salmon-pink calcite stratigraphically below the last occurrence of possible anhydrite pseudomorphs
17-BH-LL-01 278/20	N 55°48.198', W 006°07.713'	Dark grey limestone under lighter grey limestone with crumbled crack-fills of lighter grey limestone.

Table 1. Samples with plane orientation (not bedding), coordinates according to WGS84 and a short description of each sample. PAS=Port-an-t-Struthan, Bonahaven Dolomite Formation, North Islay LL= Lossit Limestone, Loch Lossit. *Exact position not noted at site, approximately 10 m west of anticline hinge where sample 17-BH-PAS-07 was taken.

3.2 Laboratory methods

The laboratory methods include five parts. The method used to prepare samples for making of thin sections is presented in section 3.2.1. Scanning electronic microscope (SEM) method is described in section 3.2.2. Microprobe analysis method is described in section 3.2.3, thin section visual analysis is described in section 3.2.4 and handheld XRF-method is described in section 3.2.5.

3.2.1 Preparation of samples for making of thin sections

The collected samples were prepared for thin section-making by cutting out chosen parts into rock chips using a rock-cutting saw. The cutting plane (β -surface) was made along mineral lineation and perpendicular to foliation in samples where such features were found. In samples without detectable lineation and foliation the cut was made where most information was thought to be found. Sample 17-BH-PAS-03 was not sent for thin section because the cutting did not show any pseudomorph-like features. Sample 17-BH-PAS-04 was used for two rock-chips; named A and B. The prepared rock chips were sent to Piotr Krzeminski, ABCahead, Poland, for making of thin sections except for sample 17-BH-PAS-08 that was made to thin section by Dan Zetterberg, Stockholm University.

3.2.2 Scanning electronic microscope

Thin sections of sample 17-BH-PAS-01, 17-BH-PAS-08 and a sample previously collected of the possible anhydrite pseudomorphs by A.Skelton; 16-NI-01, was chosen for analyse in a scanning electronic microscope (SEM). No carbon-coating was used. The thin sections were analysed by Marianne Ahlbom at Stockholm University in a FEI Quanta Feg 650 SEM using an Oxford X-max analyser. The analysed points were chosen by visual inspection of the thin sections in microscope. In sample 16-NI-01 a suspected barite crystal and different sparry calcite grains were chosen. In sample 17-BH-PAS-01 a suspected anhydrite inclusion and sparry non-striated calcite crystal were chosen. In sample 17-BH-PAS-08, three suspected anhydrite inclusions and different looking calcite crystals were chosen.

3.2.3 Thin section visual analysis

All thin sections are scanned using a Nikon Scan “Supercoolscan9000 ED” at Stockholm University. The samples are studied with a Leica microscope and photographed with a Leica EC3 camera to LAS EZ software for further study of the mineral distribution in the pseudomorphs. Other features including suspected microbial mat horizons and suspicious anhydrite inclusions in other samples were photo-documented for further study. Magnification of 2,5x, 10x, 20x and 40x were used.

3.2.4 Handheld X-ray fluorescence analysis

X-ray fluorescence (XRF) analyses were made with a handheld XRF on Stockholm University on samples 17-BH-PAS-01 (two areas), 17-BH-PAS-02, 17-BH-PAS-04 (two areas), 17-BH-PAS-05 (two areas), 17-BH-PAS-07, 17-BH-PAS-08 (three areas), 17-BH-PAS-09 (three areas), 17-BH-PAS-11 (two areas), 17-BH-11 (two areas), 17-BH-LL-01 (two areas) and 17-BH-CNU-01.

3.2.5 Microprobe analysis

Samples 17-BH-PAS-05, 17-BH-PAS-08 and 15-NI-01 were chosen for microprobe analysis at Uppsala university. Sample 17-BH-PAS-05 contains a suspected microbial mat horizon. The samples were prepared for microprobe analysis with a thick carbon-coating (9 seconds) by Marianne Ahlbom, Stockholm University. Microprobe analysis was made on a Hyperprobe JEOL JXA-8530F electron probe microanalyser by Iwona Klonowska and Jaroslaw Majka at Uppsala Geocenter. Qualitative analyses were made with an energy-dispersive X-ray spectroscope (EDS) to define present elements was made on 3 points in sample 17-BH-PAS-05, 5 points in sample 17-BH-PAS-08 and three points in sample 17-BH-PAS-01. Quantitative analysis was made with a wavelength dispersive X-ray spectroscope (WDS) on different grains in the analysed areas to define the different minerals. Different protocols were used to make the qualitative analyses depending on elements present in qualitative analyses. There were no suitable protocols available for the array of elements present for some of the mineral grains. For these mineral grains a protocol with most elements present were used; further details are presented in the result section. Secondary electron images (SEI) were taken on the organic network in sample 17-BH-PAS-05.

4 Results

4.1 Stratigraphic profile and cross-section of study area

The location of the study area and a simplified shoreline illustration is shown in figure 9 a. A simplified cross-section of the study area is presented in figure 9 b. A stratigraphic profile is presented in figure 10 a where the different sections are marked out. The profile begins at ~20 m west of the fault-defining breccia outcrop. The topmost part of section C is presented in more detail in figure 10 b. Folding along the beach makes precise correlation between section C and D uncertain, though stromatolites are absent in the topmost part of section D which could relate the first possible anhydrite pseudomorph occurrence in the beginning of section C to section D. Another possibility is that the topmost part of section C relate to section D but represent different parts of the sedimentary basin. The alternative correlations between section C and D are shown in figure 9 b.

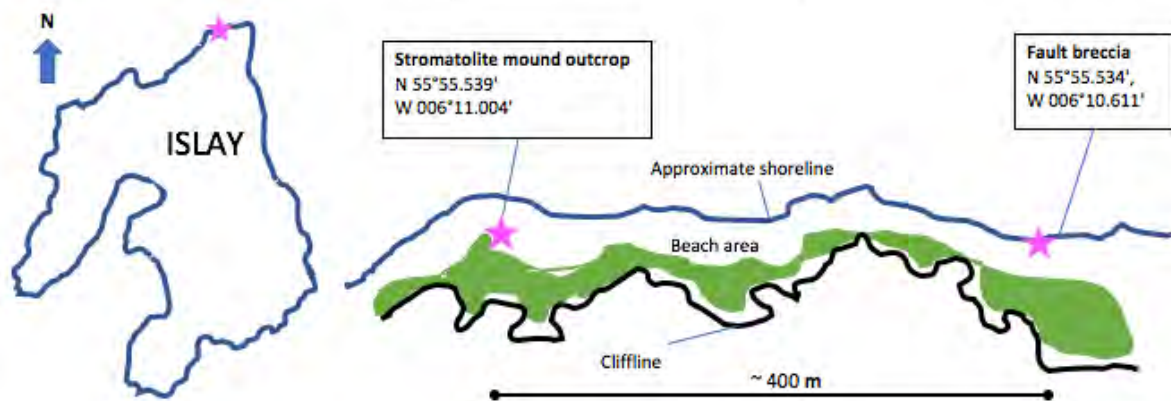


Figure 9 a). The outline of Islay and a simplified shoreline illustration of the study area. Outlines are traced from image in Google Earth.

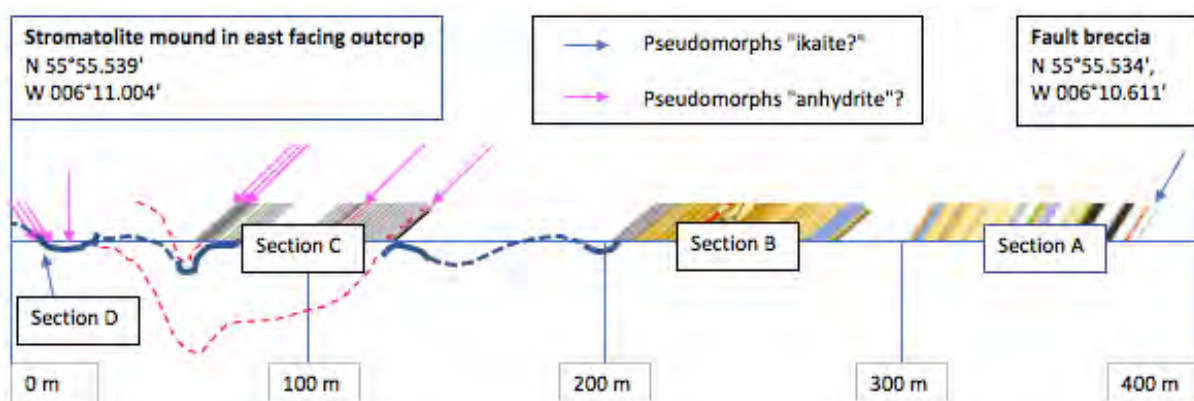


Figure 9b). Simplified cross-section of study area at Port an t-Struthain, North Islay. The blue lines show folding and correlation of layers at folding is shown with dotted lines. The red dotted lines are an alternative correlation of the first and last occurrence of the possible anhydrite pseudomorph layers. The W-E bounds of the profile is marked out with coordinates and the beds where the pseudomorphs were found are marked out. An approximate dip of the beddings is illustrated with a tilt of the sections.

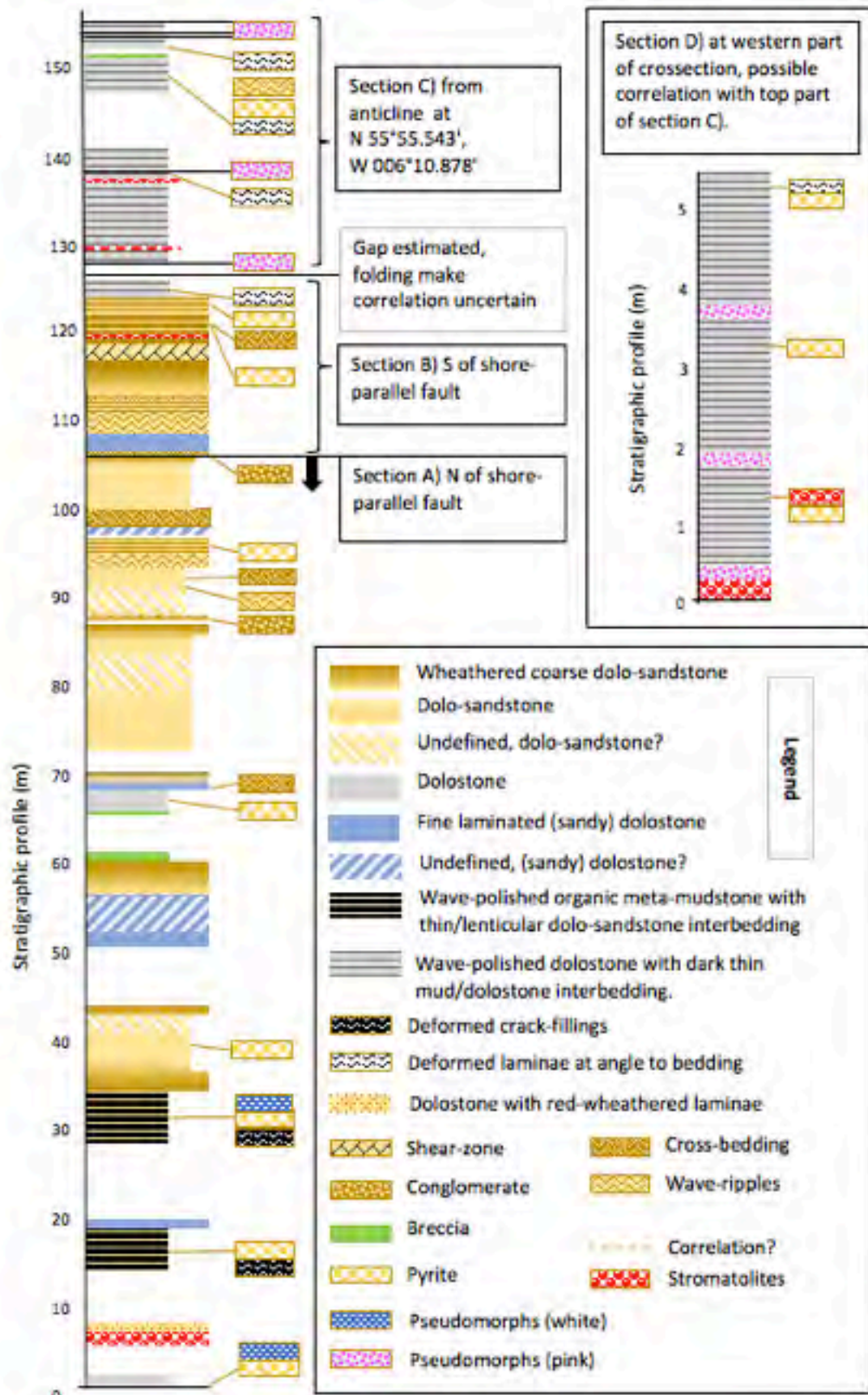


Figure 10 a. Stratigraphic profile from the possible ikaite pseudomorphs to the second sequence of possible anhydrite/gypsum pseudomorphs.

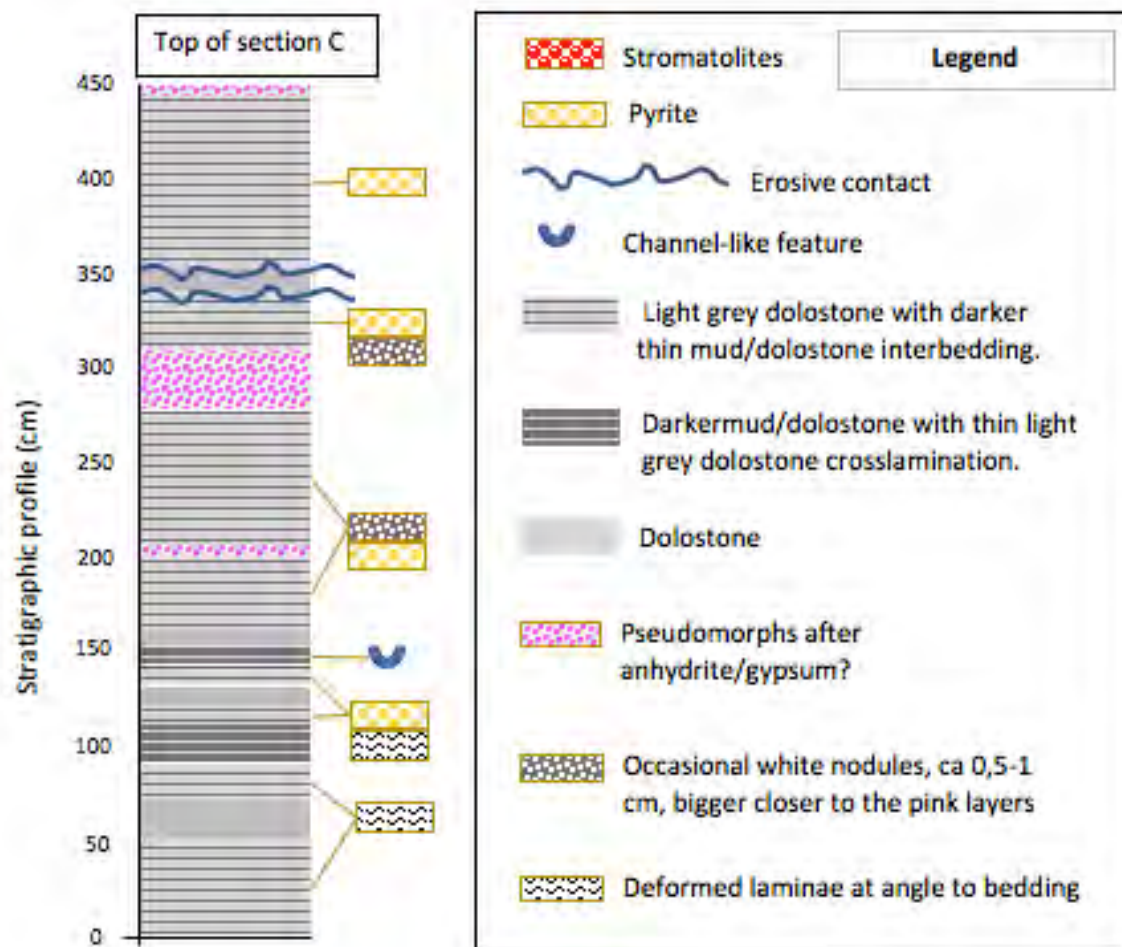


Figure 10 b. Stratigraphic profile of the top 4,5 m of sequence C.

4.2 Pseudomorphs described in thin section

The pseudomorph samples are presented in the order they occur within the stratigraphic profile. All quartz in all pseudomorphs shows undulatory extinction. Pyrite is present in different sizes in all thin sections albeit not always big enough to be visible in the scanned images. All dolostone have small white dots present and pyrite occurs in thin laminae every 0,5-15 cm. These pyrite laminae are within the dark thin mud/dolostone interbedding in the possible anhydrite pseudomorph-bearing units.

Sample 17-BH-PAS-08: The sample is from the first dolostone unit and was collected because it contained suspected ikaite pseudomorph sample. Elongate pseudomorphs ranging in size from ca 1-5 mm are distributed within the unit, see figure 11 a. The sample was analysed in scanning electron microscope (SEM) and microprobe. A scanned image of the thin section with the analysed areas marked out is presented in figure 11 b. Analysed inclusions were confirmed as anhydrite in both a pyrite and a quartz crystal. The pseudomorphs have an estimated mineral composition of 10 % pyrite, 55-70% quartz and 20-35% carbonate. Edges are often microcrystalline and interiors sparry. Pyrite is mostly distributed in the microcrystalline areas.



Figure 11 a). First unit of wave-polished dolostone with elongate aligned pseudomorphs (dark arrow pointing at one of them) with small white grains/dots (white arrows pointing at two of them). Sample 17-BH-PAS-08 is from this unit. Pyrite laminae have a slight rusty tint and very small pyrite crystals.



Figure 11 b) Scanned image under crossed polar of sample 17-BH-PAS-08 thin section. The white arrow points at the pyrite crystal with the analysed inclusion. The red arrow points at the quartz grain with the analysed anhydrite inclusion. The blue arrow points at the analysed dolomite crystal area. The pseudomorph with the analysed areas is outlined with red dotted line.

Sample 17-BH-PAS-01: The sample was collected from the organic meta-mudstone with thin/lenticular dolo-sandstone interbedding because it contained possible ikaite pseudomorphs. The meta-mudstone beds show frequently occurring cracks that are filled with dolo-sandstone from above and appear deformed from compaction. Within the dolo-sandstone there are abundant pseudomorphs with a high pyrite content, see figure 12 a. Carbonate and small inclusions in pyrite in the largest pseudomorph were analysed in scanning electron microscope. None of the analysed inclusions were confirmed as anhydrite and they do not resemble the confirmed anhydrite inclusion either. Results are presented in table 3 in section 4.3. A scanned electron image of the thin section is presented in figure 12 b where the SEM-analysed area is marked out and two pseudomorphs are outlined. The mineral composition of

the pseudomorphs of this sample and a sample collected from the same unit by Christina Ohrazda (sample 17-CO-PAS-03) vary strongly in mineralogy with carbonate 0-20%, pyrite 20-80% and quartz 20-65%. The pyrite are often the largest crystals and occur in clusters. The edges are often ill defined and do not display microcrystalline quartz. In some pseudomorphs the quartz crystals are elongate in the direction of mineral alignment in the matrix. Inclusions similar to the confirmed anhydrite inclusion are present in sample 17-CO-PAS-03.



Figure 12 a). Organic metamudstone with thin/lenticular dolo-sandstone. Red arrow points out one crumbled crackfill and green arrow points at one of the pyrite-clotted pseudomorphs. Inset show beddingplane just above where sample 17-BH-PAS-03 was taken. Pen for size.



Figure 12 b) Scanned image of sample 17-BH-PAS-01. The area that was analysed in SEM is marked out with a red square. The green arrows point at the two largest pseudomorphs which are outlined with red dotted line. The blue arrow points at a crackfill.

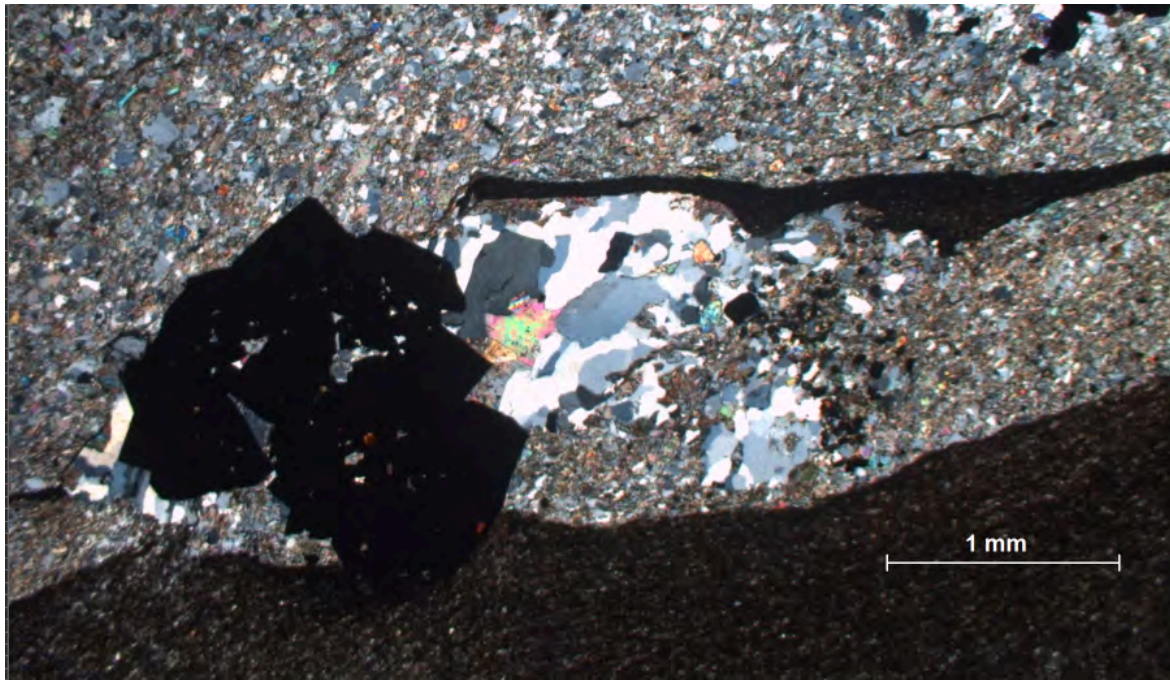


Figure 12 c). The largest of the pseudomorphs in sample 17-BH-PAS-01. Dark area below is organic-rich fine-grained metamudrock and the coarser, lighter coloured matrix is dolo-sandstone that have also filled the space underneath the pseudomorph which lies in the top of a deformed crackfill. The image is slightly tilted to the left compared with figure 12 b.

Sample 17-BH-PAS-02: The sample is from a unit of fine laminated sandy dolostone on top of section A (correlated with the only unit of this lithology in section B). Both the lamination and the manner in which the rock fractures where this lithology is brecciated at the surface are similar to quartzite. Values from hand-held XRF presented in section 4.5 show that the Ca-concentration is three times higher (20,9 wt%) than the Si-value (6,7wt%). Where pyrite is detected in this lithology it occurs in very fine laminae. A narrow vein in the sample contains a few fluorite grains.

Sample 17-BH-PAS-07: The sample was collected from a conglomerate which comprises elongate “pebbles”, see figure 13 (left). The composition is approximately 80% carbonate and 20% quartz with minor pyrite present. The edge of the pseudomorph has a broad area of microcrystalline quartz followed by a coarser quartz and sparry carbonate towards the interior. Inclusions that are similar to the confirmed anhydrite inclusions in sample 17-BH-PAS-08 are present, see figure 13 (right).

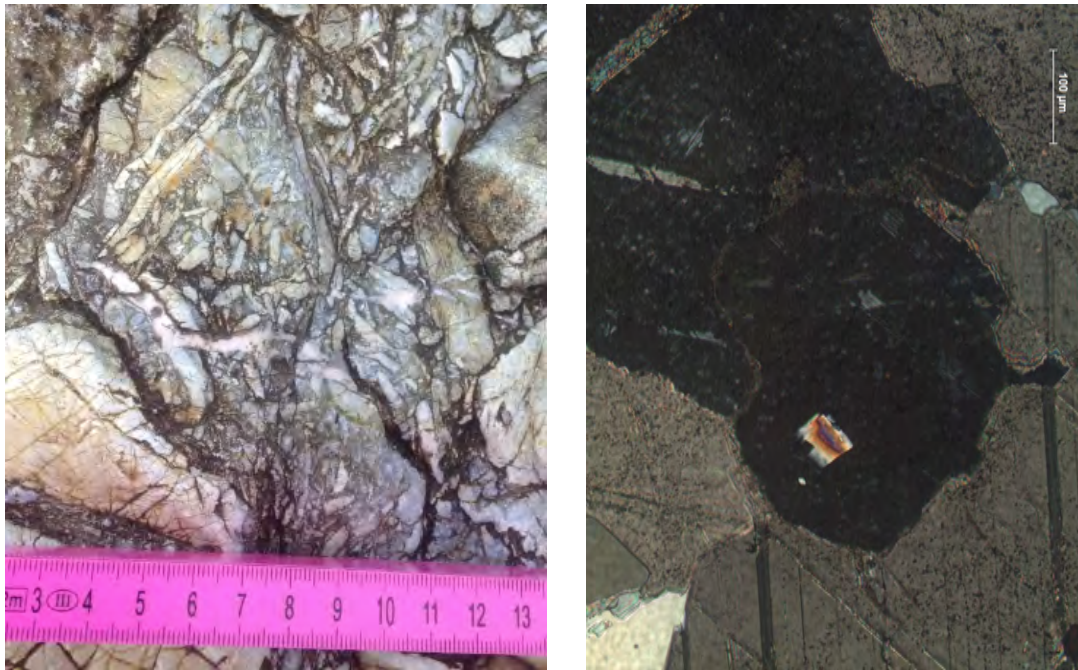


Figure 13. The “hinge conglomerate” with elongate pebbles (left) and inclusion (right).

Sample 17-BH-PAS-06: The sample was collected as a first occurrence of possible anhydrite pseudomorphs. The pseudomorph is larger than the thin section and the visible part have a narrow microcrystalline quartz edge with pyrite crystals distributed within. The interior of the pseudomorph comprises sparry carbonate with a few coarse quartz crystals. Estimated mineralogy comprises 80% carbonate and 20% quartz with minor pyrite content. Inclusions that are very similar to the analysed anhydrite inclusions are present. The rim is microcrystalline with pyrite forming an inner rim, whereas the core is made of sparry carbonate and quartz (figure 14).

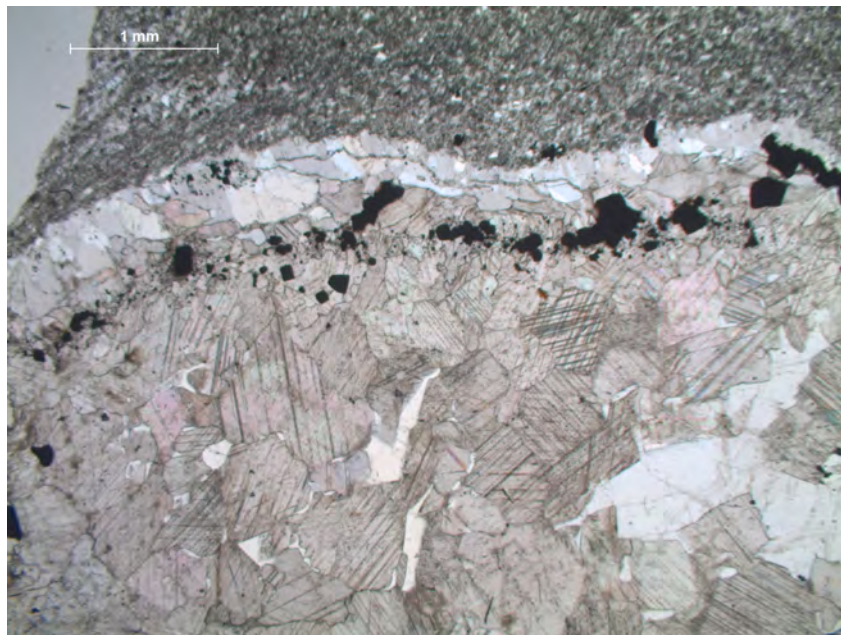


Figure 14. The microcrystalline rim with pyrite mostly inside. Sparry carbonate and occasional quartz (white) inside.

Sample 17-BH-PAS-04: The sample contains possible anhydrite pseudomorph from one of the pink pseudomorph layers in the top of section C. Two thin sections were made from this sample, 17-BH-PAS-04A and 17-BH-PAS-04B (figure 15 a). The pseudomorph in A is much larger than the thin section and continue above and below. Edges are defined by microcrystalline quartz. Coarse quartz crystals have grown inwards and the void space is filled by carbonate. Sparry carbonate also fills the remaining area of the pseudomorph. Small angular inclusions with high birefringence resembling the confirmed anhydrite inclusion are present in both carbonate and quartz grains in both thin sections. One inclusion in a quartz grain is shown in figure 15 b. The carbonate grains in the image show a speckled texture and appears zoned. The speckled texture is similar to that of the analysed dolomite grains in sample 17-BH-PAS-08. In 17-BH-PAS-04B B there is a microcrystalline outline of what can be a separate, smaller pseudomorph. The mineralogy in this pseudomorph (-part) is ca 40 % quartz and 60% carbonate, with minor pyrite grains present in the microcrystalline quartz rim.

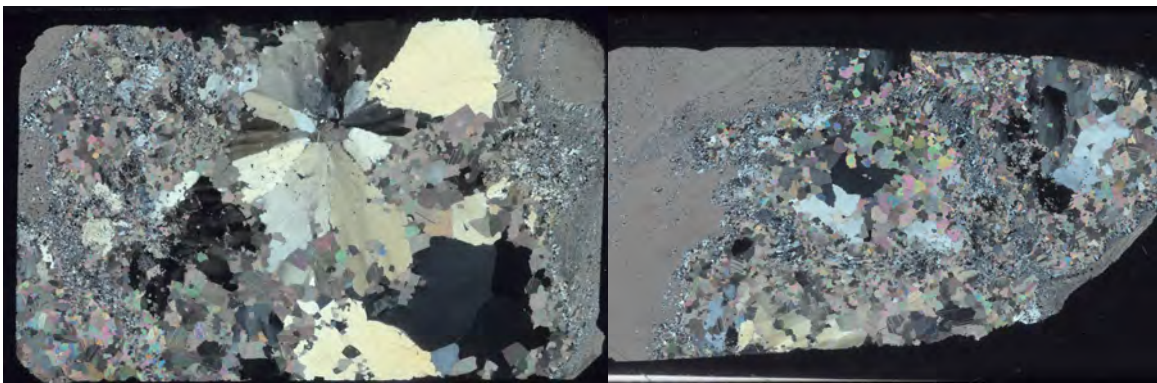


Figure 15 a). Scanned images of sample 17-BH-PAS-04A (left) and 17-BH-PAS-04B (right) in thin section. The samples are a possible anhydrite pseudomorphs.



Figure 15 b). Sharply pink/purple square inclusion in coarse quartz grain (dark area in image) in upper edge of thin section 17-BH-PAS-04B. The image is zoomed in on the scanned image.

Sample 17-BH-PAS-09: The sample was collected from the uppermost layer with possible anhydrite pseudomorphs in the western end of the study area. A cut sample show an elongate shape of the pseudomorphs. The pseudomorphs have a sparry interior of carbonate and quartz. The mineral composition is approximately 53% sparry carbonate, 32 % sparry quartz and 15% intermingled microcrystalline quartz and carbonate. Almost no pyrite is present within the interior but is found within the nearby matrix. A scanned image of the thin section is shown in figure 16 (left). Inclusions similar to the confirmed anhydrite inclusion in sample 17-BH-PAS-08 are present, see figure 16 (right).

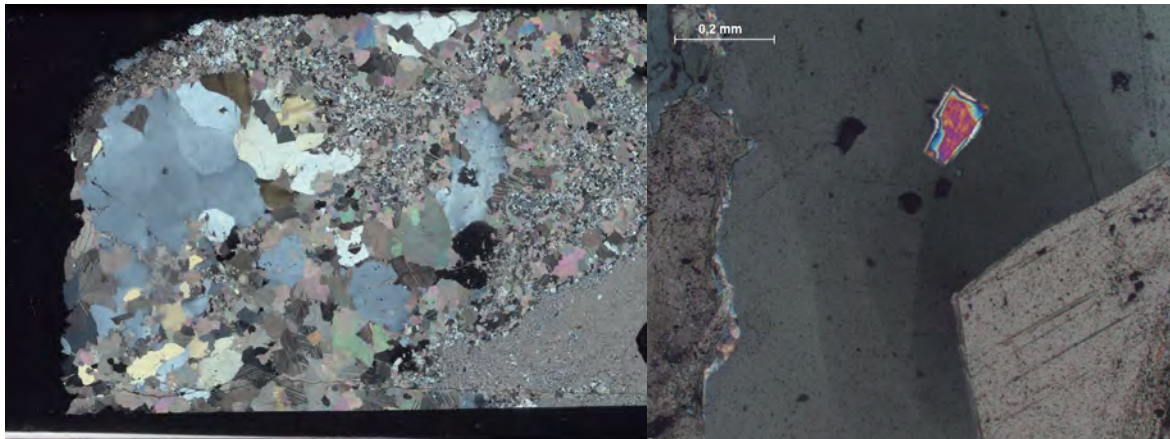


Figure 16. Scanned image of thin section for sample 17-BH-PAS-09 (left). An inclusion in the sparry quartz crystal in the right part of the scanned image (right).

Sample 15-NI-01: The sample is collected by Alasdair Skelton from one of the possible anhydrite pseudomorph bed in the western part of the study area. Suspected barite crystals were analysed in both scanning electron microscope and microprobe and were confirmed as barite. An inclusion in a quartz crystal was analysed using the microprobe and was confirmed as anhydrite. A scanned image of the thin section of the sample is presented in figure 17.

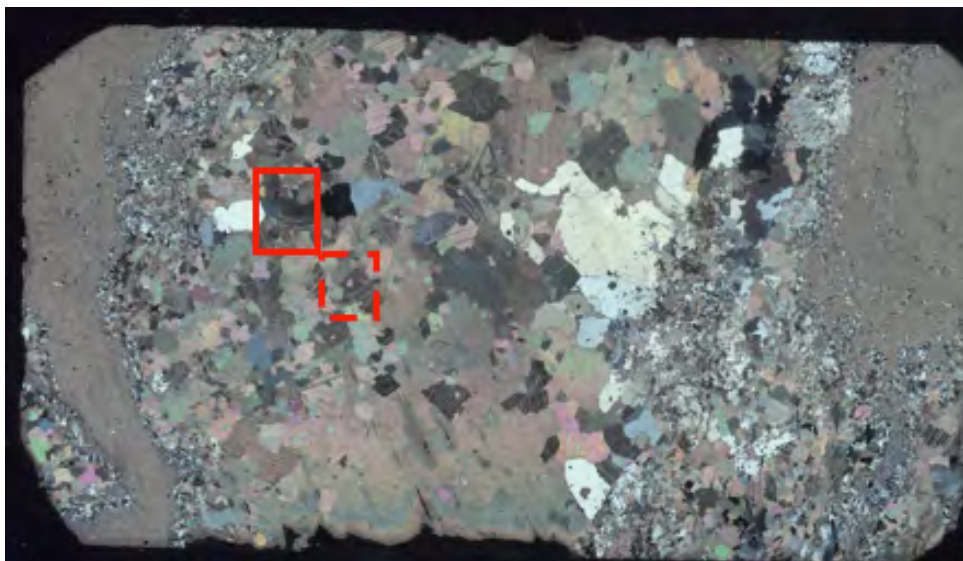


Figure 17. Scanned image under crossed polars of sample 16-NI-01 thin section. Red line is the area with the barite crystals. The dotted line is the area where calcite crystals were analysed.

Samples 17-BH-PAS-10 and 17-BH-PAS-11: The samples are from veins in the western end of the study area. The composition is mostly sparry quartz and carbonate. These sample were collected for comparing purpose. The crystals have almost no inclusions compared to the crystals of the pseudomorphs which have very abundant inclusions of different mineralogy.

4.3 Possible microbial mat microfossils described in thin section

Sample 17-BH-PAS-05: The sample was collected as a suspected microbial mat surface west of the study area, though from a bed which is included in the stromatolite mound outcrop at the western end of the study area. The bedding plane has a tufty surface, see figure 18 a. This surface is very similar to the described tufty surfaces of microbial mats that can be preserved as microbially induced sedimentary structures (Noffke et al., 2013) as described in section 1.2.2. A microscope image with 40x enlargement is presented in figure 18 b. As parts of the surface crumbled away when cutting the rock, the rock chip was glued with epoxy by Dan Zetterberg, Stockholm University, before sending for making of thin section. The sample was analysed in microprobe and the organic looking network under the bedding plane surface have a very high carbon content confirming an organic origin.

A secondary electron image showing the organic network is presented in figure 18 c. The dolomite matrix beneath the organic network contains larger crystals of quartz, grains of K-feldspar, muscovite and apatite and thin calcite veins.



Figure 18 a). The tufty surface of the bedding plane of which the sample was taken. The surface tended to be damaged by cutting (left). The surface in field, pencil for size.

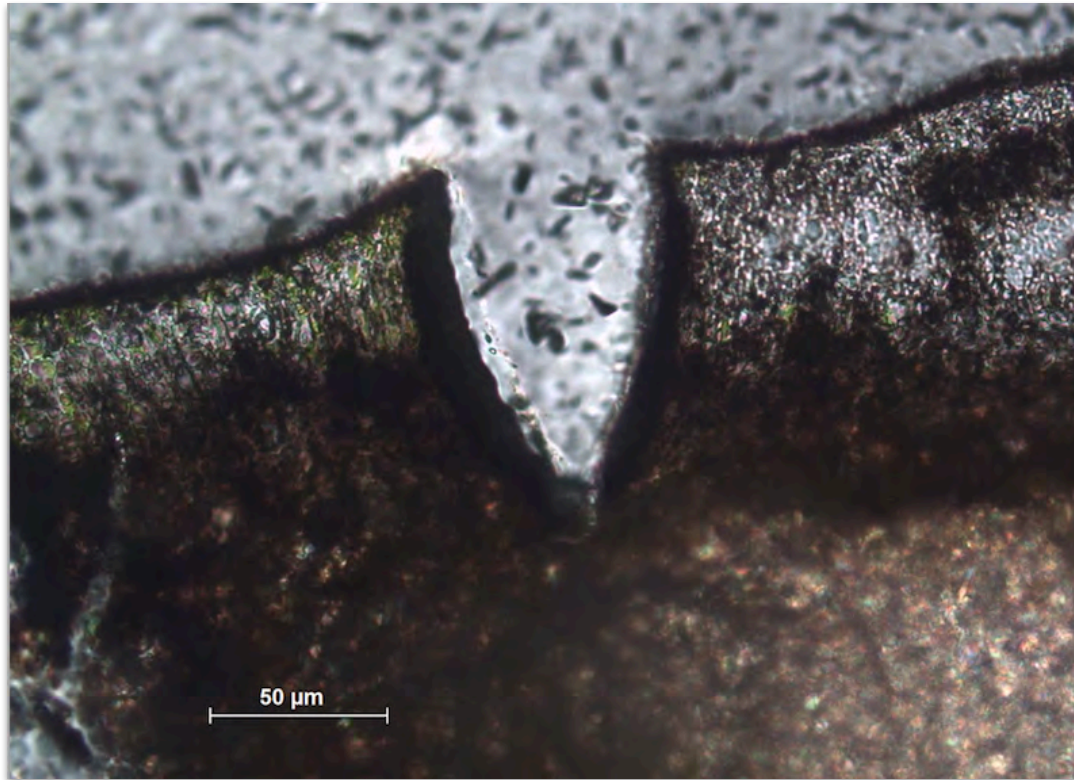


Figure 18 b). Microscope image of suspected fossil microbial mat surface in profile. The grainy area above is epoxy. The V-shape with slightly bent-up edges strongly resembles the cracking and curling up of edges of a drying microbial mat. The “furry” uppermost surface is most probably on-growth of lichen. The texture beneath the dark outlined surface have filament-looking lines that separate what looks like very small faintly pink grains.

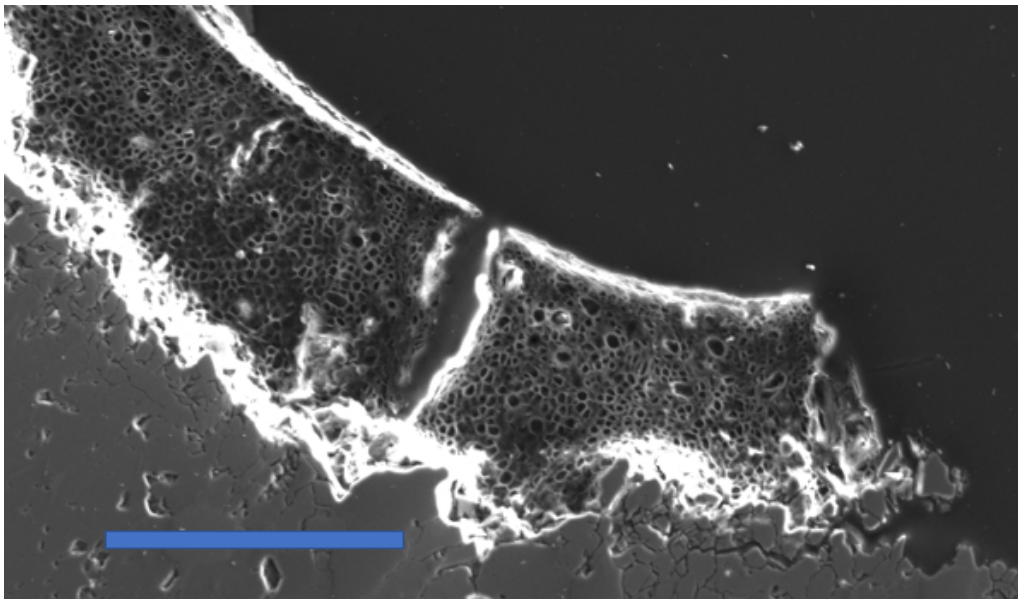


Figure 18 c). Close-up of secondary electron image of the organic network in sample 17-BH-PAS-05. The spaces within the network that looked like faintly pink grains in figure 18 b are empty. Original image taken by Iwona Klonowska, Uppsala University. Scalebar 100 μm.

Sample 17-BH-LL-01: The sample was taken in the Lossit Limestone close to Loch Lossit on north Islay. This formation is not a part of the study but the sample show dark thin layers that look organic and might be of microbial origin. Figure 19 shows two irregular dark lines and a close-up of one of them.

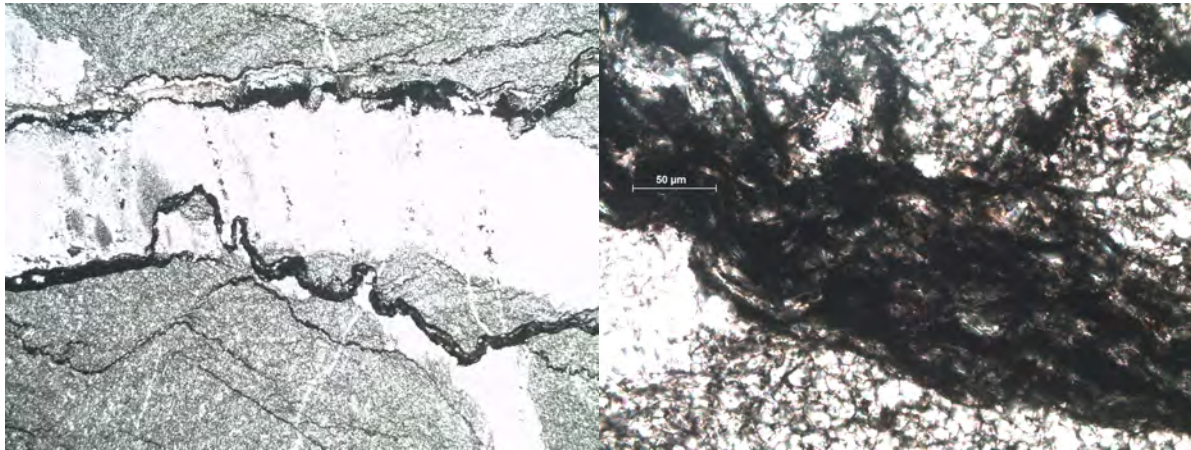


Figure 19. Two organic-rich very thin horizons and a close-up image of one of them.

4.4 Scanning electronic microscope (SEM) results

The results of the scanning electronic microscope analyses at Stockholm University are presented in table 3, where known values for each suspected mineral is shown in different colours to compare with in table 2 (webmineral.com). Table 3 shows each sample separately. Normalized values from the sample of elements present in the suspected mineral are presented where the values not match directly. The normalized values are presented according to the colour-scheme in table 2.

Known values	Elements (wt%)							
	O	S	Ca	Fe	Si	C	Mg	Ba
anhydrite	47,01	23,55	29,44					
pyrite		53,45		46,55				
calcite	47,96		40,04			12,00		
dolomite	52,06		21,73			13,03	13,18	
Known barite	27,42	13,74						58,84
Known quartz	53,26				46,74			

Table 2. Known values of elements in wt% of occurring minerals (webmineral.com)

Sample 17-BH-PAS-08									
	Suspected mineral	Elements wt%/ σ							
		O	S	Ca	Fe	Si	C	Mg	others
1	anhydrite	41,6/ 0,4	23,1/ 0,2	20,9/ 0,2	5,6/ 0,1	5,0/ 0,1	3,7/ 0,5		
	Norm.	48,6	27,0	24,4					
2	pyrite	9,2/ 0,3	42,5/ 0,4	0,3/ 0,0	36,5/ 0,4	5,0/ 0,1	6,5/ 0,7		
	Norm.		53,8		46,2				
3	calcite	49,2/ 0,3		25,2/ 0,2	0,2/ 0,0	8,0/ 0,1	17,2/ 0,3	0,3/ 0,0	
4	quartz	51,5/ 0,3		0,8/ 0,0		44,3/ 0,3	3,3/ 0,4		
5	anhydrite	46,4/ 0,3	17,0/ 0,1	20,9/ 0,2	0,2/ 0,1	11,0/ 0,1	3,9/ 0,4	0,5/ 0,0	
	Norm.	55,0	20,2	24,8					
6	quartz	51,1/ 0,3		1,7/ 0,1	0,3/ 0,1	41,9/ 0,3	4,4/ 0,4	0,5/ 0,0	
7	Dolomite/	49,1/ 0,3		20,5/ 0,1	2,5/ 0,1	4,1/ 0,1	14,3/ 0,3	9,6/ 0,1	
8	high Mg-	49,0/ 0,3	0,1/ 0,0	22,4/ 0,1	3,5/ 0,1	1,4/ 0,0	13,7/ 0,3	9,8/ 0,1	
9	calcite	49,3/ 0,3	0,1/ 0,0	22,2/ 0,1	3,3/ 0,1	1,7/ 0,0	13,6/ 0,3	9,8/ 0,1	
10		48,9/ 0,3		22,4/ 0,2	3,4/ 0,1	1,3/ 0,0	13,9/ 0,3	9,7/ 0,1	Al 0,1/ 0,0 Mo 0,3/ 0,1
11		49,9/ 0,3		22,2/ 0,1	1,7/ 0,1	1,0/ 0,0	13,6/ 0,3	11,6/ 0,1	
12		49,3/ 0,3		22,4/ 0,1	2,9/ 0,1	1,2/ 0,0	13,7/ 0,3	10,3/ 0,1	Al 0,1

Sample 15-NI-01									
	Suspected mineral	Elements wt%/ σ							
		O	S	Ca	Ba	C	Sr	Si	others
13	barite	26,0/ 0,3	12,3/ 0,1	2,3/ 0,1	52,4/ 0,3	4,6/ 0,4	2,0/ 0,2	0,4/ 0,1	Co 0,1/ 0,1
	Norm.	28,67	13,56		57,78				
14	barite	27,2/ 0,3	12,2/ 0,1	2,2/ 0,1	50,7/ 0,3	4,5/ 0,4	2,3/ 0,2	0,8/ 0,1	
	Norm.	30,19	13,54		56,27				
15	calcite	46,5/ 0,3	0,4/ 0,0	37,2/ 0,2	1,9/ 0,1	13,3/ 0,2		0,2/ 0,0	Fe 0,2/ 0,1 Mg 0,3/ 0,0
16	Quartz (+calcite)	50,2/ 0,3	0,2 (0,0)	2,2/ 0,1	1,1/ 0,1	6,1/ 0,5		40,3/ 0,3	
	Norm.	55,47						44,53	
		O	Ca	Mg	Fe	C		S	
22	calcite	46,9/ 0,3	39,7/ 0,2	0,2/ 0,0	0,2/ 0,1	12,9/ 0,2			
23		47,0/ 0,3	39,2/ 0,2	0,5/ 0,0	0,3/ 0,1	13,0/ 0,2			
24		46,7/ 0,3	39,5/ 0,2	0,5/ 0,0	0,2/ 0,1	13,1/ 0,2			
25		47,0/ 0,3	38,7/ 0,2	0,5/ 0,0	0,4/ 0,1	13,5/ 0,2			
26	pyrite (+ calc.+ organic?)	11,0/ 0,3	10,5/ 0,1		28,3/ 0,3	17,6/ 0,7			32,7/ 0,3
	Norm.				46,39				53,61
	Norm.	28,1	26,9			45			

Sample 17-BH-PAS-01									
		Elements wt%/ σ							
		O	S	Ca	Fe	Si	C	Mg	others
27	Dolomite/ high Mg-calcite	46,9/ 0,3	1,2/ 0,0	20,9/ 0,2	3,0/ 0,1	4,8/ 0,1	14,3/ 0,4	8,6/ 0,1	Al 0,2/ 0,0 K 0,1/ 0,0
	Norm. sample	51,7		23			15,8	9,5	
28	Dolomite/ high-Mg calcite	43,2/ 0,3	2,4/ 0,0	21,7/ 0,2	8,0/ 0,1	4,2/ 0,1	14,3/ 0,4	5,9/ 0,1	Al 0,3/ 0,0 K 0,1/ 0,0
	Norm. sample	50,8		25,5			16,8	6,9	
29	Pyrite + quartz + calcite+ carbon?	33,4/ 0,4	20,3/ 0,2	1,3/ 0,1	16,7/ 0,2	22,8/ 0,2	4,5/ 0,8	0,5/ 0,0	Al 0,4/ 0,0 K 0,2/ 0,0
	Norm. sample		54,9		45,1				
	Norm. sample	59,4				40,6			
30		42,4/ 0,4	10,0/ 0,1	0,8/ 0,0	7,8/ 0,1	34,1/ 0,3	4,1/ 0,7	0,3/ 0,0	Al 0,2/ 0,0 K 0,2/ 0,0
31	Pyrite + quartz + calcite + carbon?	14,8/ 0,3	36,9/ 0,3	1,3/ 0,1	30,6/ 0,3	7,8/ 0,1	7,3/ 0,7	0,6/ 0,1	Al 0,3/ 0,0 Ni 0,4/ 0,1
	Norm. sample		54,7		45,3				
	Norm. sample	65,5				34,5			
32	quartz	50,1/ 0,4	0,8/ 0,0	0,7/ 0,0	0,7/ 0,1	44,2/ 0,4	2,7/ 0,6	0,2/ 0,0	Al 0,4/ 0,0 K 0,2/ 0,0

Table 3. Scanning electron microscope results of samples 17-BH-PAS-08, 16-NI-01 and 17-BH-PAS-01. In spectra that do not directly correlate with any of the known mineral values, a normalization of the element values for that mineral is normalized from the sample values. At some spectra there are very mixed values, this can be because there are small inclusions that can get influenced by the surrounding minerals. Norm. = normalized values from the sample to compare with the suspected mineral. Red = anhydrite, green=pyrite, blue = calcite, purple = dolomite, grey = quartz, brown = barite.

4.5 Microprobe analysis results

The results of the microprobe analyses made at Uppsala Geocentrum are presented in table 4 a and 4 b. The qualitative analyses of the network in sample 17-BH-PAS-05 (run 1 in table 4 b) gave a low total result because it mainly consists of carbon. The results of the quantitative analyses for the organic network is therefor included in table 3 b. The analysed inclusion in pyrite and the dolomite area in sample 17-BH-PAS-08 are the same as in the SEM-analyses. The analysed barite in sample 15-NI-01 is the smaller of the two barite-grains shown in figure 18 a, the anhydrite inclusion is within a quartz grain closer to the left microcrystalline edge. The calcite is a calcite grain adjacent to the barite.

Wt%	Sample 17-BH-PAS-08					Sample 15-NI-01		
	4 (dol)	5 (dol)	6 (dol)	7 (dol)	8 (anh)	9 (bar)	10 (anh)	11 (cal)
Na ₂ O						0,17		
SiO ₂	0,0331						0,186	
Al ₂ O ₃						0,252	0,014	
MgO	14,787	14,565	14,018	15,544				0,591
CaO	30,367	30,717	30,889	28,695	40,91	0,021	41,909	52,806
NiO					0,0885			
FeO	3,136	3,02	3,67	2,038	0,6269			0,332
MnO		0,013		0,092	0,0041			0,063
Cr ₂ O ₃					0,0025			
V ₂ O ₃					0,0053			
BaO	0,047	0,027	0,059			67,9	0,072	
F					0,116			
SrO	0,041	0,089	0,045	0,094		3,016	0,56	0,11
CO ₂	41,028	41,911	41,829	40,835		77,316	126,747	42,376
SO ₃					38,72	34,008	65,58	
Total:	90,3061	90,342	90,51	87,2981	80,5065	182,683	226,068	96,2781

Table 4 a). Qualitative microprobe analysis results for sample 17-BH-PAS-08 and 16-NI-01. The CO₂ values written in grey on run # 9 and 10 can be ignored because a protocol was used that includes C which take the carbon coating into account (Jaroslaw Majka, personal communication, May 4, 2017). Dol= dolomite, anh= anhydrite, bar=barite, cal=calcite.

Sample 17-BH-PAS-05				Quantitative		
Chemical formula (wt%)	1 organic network	2 K-Feldspar	3 muscovite	Organic network (not same spot as qualitative analysis)		
				Chem. Form.	Mass%	Mol%
Na ₂ O	0,386	0,3394	0,0753	C	53,59	86,15
SiO ₂	2,457	65,05	49,4	Na ₂ O	0,76	0,24
Al ₂ O ₃	0,267	18,29	25,63	MgO	1,81	0,24
MgO	0,921	0,0348	4,36	Al ₂ O ₃	1,00	0,19
K ₂ O	0,084	15,76	11,07	SiO ₂	6,16	1,98
P ₂ O ₅	2,351			P ₂ O ₅	1,58	0,21
CaO	5,729	0,1083	0,3184	SO ₃	5,80	1,40
TiO	0,008	0,0206	0,512	CaO	14,38	4,95
NiO	0,092			FeO	14,93	4,01
FeO	3,437	0,0429	2,31			
MnO	0,077	0,0084				
Cr ₂ O ₃	0,046		0,0317			
V ₂ O ₃	0,04		0,0761			
BaO		0,4331	0,1275			
F			0,0306			
Total:	15,895	100,0874	93,9417			

Table 4 b). Qualitative and quantitative analyses for sample 17-BH-PAS-05. In run #1 there is S present too but a protocol was used that do not include S. The low total is because of high C-content which is not included in the protocol used. This choice was made because there were no suitable protocol including both S, C and all other present elements (Iwona Klonowska, personal communication, May 4, 2017).

4.6 Handheld XRF-results

Handheld XRF-results for elements with higher content than 0,5 wt% in the sample are presented in table 5.

Sample (area)	Mg/ Mg +/-	Al/ Al +/-	Si/ Si +/-	K/ K +/-	Ca/ Ca +/-	Fe/ Fe +/-
17-BH-PAS-01 (dark matrix)		5,71/ 0,1	21,12/ 0,11	5,30/ 0,0273	3,32/ 0,0197	2,95/ 0,0049
17-BH-PAS-02 (matrix)	8,32/ 0,64	2,32/ 0,08	6,99/ 0,07	1,40/ 0,0134	20,89/ 0,17	1,32/ 0,0156
17-BH-PAS-04 (pink)			7,5/ 0,06		38,16/ 0,16	
17-BH-PAS-04 (matrix)	3,91/ 0,61	2,82/ 0,08	12,09/ 0,11		16,39/ 0,13	2,26/ 0,023
17-BH-PAS-05 (matrix)	3,24/ 0,81	1,09/ 0,08	7,95/ 0,1	0,91/ 0,0117	19,07/ 0,19	1,93/ 0,025
17-BH-PAS-05 (tufty surface)		1,06/ 0,12	3,73/ 0,09		9,95/ 0,18	1,82/ 0,0377
17-BH-PAS-07 (pink/trnsp)			19,14/ 0,1		22,46/ 0,09	
17-BH-PAS-08 (matrix)	4,01/ 0,68	2,58/ 0,09	13,37/ 0,13	2,42/ 0,0228	12,47/ 0,11	2,23/ 0,0239
17-BH-PAS-08 (nod/matrix)	3,39/ 0,79	1,26/ 0,08	19,44/ 0,2	1,28/ 0,0192	10,82/ 0,1	2,31/ 0,0276
17-BH-PAS-09 (matrix)	5,02/ 0,63	2,02/ 0,08	11,32/ 0,1	1,66/ 0,0153	19,33/ 0,15	1,8/ 0,0201
17-BH-PAS-09 (pink)			1,33/ 0,027		46,08/ 0,2	
17-BH-PAS-09 (transparent)			41,16/ 0,15		0,94/ 0,009	
17-BH-PAS-11 (pink)			6,55/0,0481		41,8/ 0,16	
17-BH-PAS-11 (matrix)	6,93/ 0,64	0,94/ 0,06	7,47/ 0,08		24,33/ 0,2	1,7/ 0,0201
17-BH-LL-01 (dark grey)			2,31/ 0,033		44,79/ 0,2	
17-BH-LL-01 (light grey)			0,74/0,0226		47,56/ 0,2	

Table 5. Results from handheld XRF-analyses.

5 Discussion of the results

5.1 Stratigraphic profile

The total thickness of the stratigraphic profile in this study is approximately 150 m; which does not include the complete succession of member 3 as described by Fairchild (1991b). The total thickness of member 3 at the study area described by Fairchild (1980a, 1991b) is ~90m. Different outcrops are included in the different studies. This study focuses on the shoreline while Fairchild's (1980a, 1991b) also includes the cliffline outcrops. Section A before the shore-parallel fault in this study has not been included in the description of member 3 in Fairchild (1991b) study of the same part of the shore. The organic meta-mudstones present in section A in this study are missing in Fairchild's (1980) description of member 3 of the BDF but are present in Fairchild's (1991a) description of member 1.

The member 1 units described by Fairchild (1991a) are at outcrops of the BDF on the northeast coast of Islay at Caol Ila and the Bunnahabhain distillery, see figure 19. The thickness of the units vary strongly already between those two sites. The study area of this project is ca 5 km from the Bunnahabhain distillery which is the closets of the two described sites (Fig. 19). A further lateral variation in thickness of the units could be expected at this further distance. A possible correlation between the stratigraphic profile in this study and Fairchild's (1991a) description of member 1 and 2 and a simplified reconstruction of member 3 (Fairchild 1991b) is presented in figure 20. The layered facies as described by Fairchild (1980a) is in this study named "dolostone with dark thin mud/dolostone interbedding"



Figure 19. The position of the study area on north Islay compared to the positions of Bunnahabhain Distillery and Caol Ila where the units of member 1 is described by Fairchild (1991 a).

The stromatolite mound outcrop at the west end of the study area correlate with one of the stromatolite layers in section D, although in the chemically weathered outcrop there were no possible anhydrite pseudomorphs identified. This do not necessarily mean that pseudomorphs are not present. The bed where sample 17-BH-PAS-06 was collected was nearly missed because the surface of the pseudomorphs were nearly covered by a dark oxidized surface.

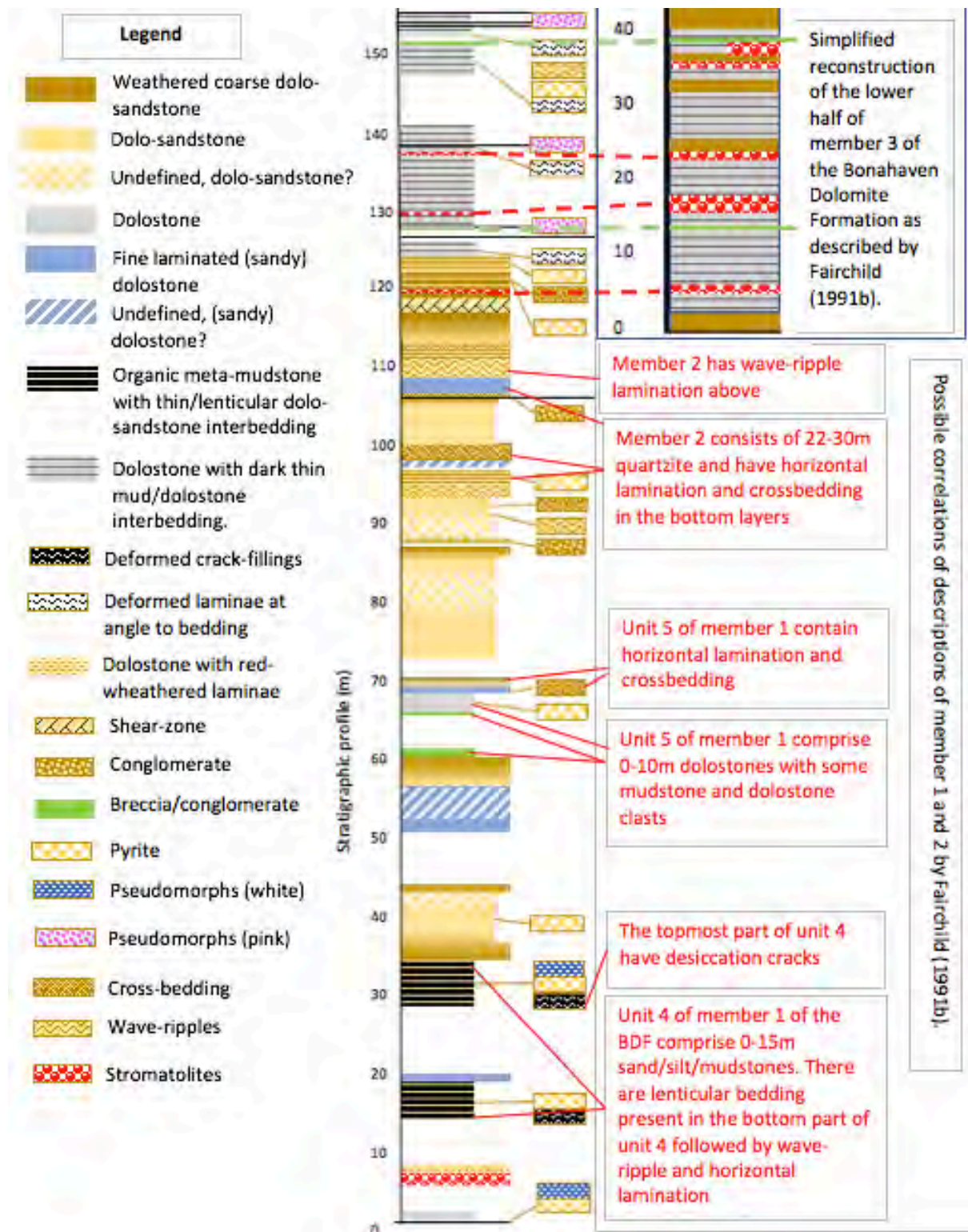


Figure 20. Possible correlation between the first 110 m of the stratigraphic profile from this study and descriptions of member 1 (unit four and five) and member 2 as described by Fairchild (1991a). The red dotted lines mark possible correlation with the features highlighted in red. Possible correlation between the top 40 m of the stratigraphic profile from this study and a simplified reconstruction of the first 40 m of member 3 as described by Fairchild (1991b). Stromatolites correlated with red dotted lines and conglomerate/breccias correlated with green dotted lines.

5.2 Pseudomorphs

Inclusions confirmed as anhydrite in sample 17-BH-PAS-08 and 16-NI-01 appear in all types of sampled pseudomorphs and suggest a calcium sulphate mineral has been replaced in all cases. This includes pseudomorphs thought to represent replacement of ikaite at the outset of this study. The likeness of ikaite pseudomorphs to lenticular gypsum in profile is emphasized in section 1.3. The carbonate content of around 1/3 expected for an ikaite pseudomorphs present in some pseudomorphs is not an indicator for ikaite in this case. This case is not unique regarding the confusion of ikaite pseudomorphs and calcium sulphate. What was interpreted as possible ikaite pseudomorphs which contrasted to overlying anhydrite/gypsum pseudomorphs in the late Cryogenian Macdonaldryggen member in NE Spitsbergen, Svalbard, turned out to originally have been calcium sulphate too (Fairchild et al. 2016).

The elongate shapes displayed in cut surfaces (figure 21 a) of the samples collected as possible anhydrite pseudomorphs (further on referred to as type 1 pseudomorphs) suggest gypsum origin that dehydrated into anhydrite by burial, leaving “ghost gypsum” (Warren, 2016). The microcrystalline quartz edges indicate dissolving and replacement mediated by sulphate reducing bacteria (SRB) during early burial; the process is described in section 1.3.2 about anhydrite and gypsum (Warren, 2016). The replacement was likely accompanied by SRB mediated pyrite formation since the pyrite is distributed together with the microcrystalline quartz; this process is described in section 1.2.2. The interior with coarse quartz, sparry calcite and barite suggests later dissolution and replacement of the main part of the anhydrite by metamorphic fluids also described in section 1.3.2.

Pseudomorphs in a cut surface of sample 17-BH-PAS-08 (type 2) have un-distorted lenticular gypsum shapes (figure 21 b). This suggests an early replacement by silica that can preserve the crystal shape and leave compressional drapes around the crystal shape (Warren, 2016). The microcrystalline edges with pyrite within and the carbonate confirmed as dolomite indicate dissolution and replacement mediated by SRB as with the type 1 pseudomorph edges. Some of the pseudomorphs in sample 17-BH-PAS-08 (figure 21 b) have open voids in the middle. These voids could form where any remaining calcium sulphate have completely dissolved in a later stage of burial and the sparry quartz crystals growing inwards did not fill the entire space (Warren, 2016) The low total of only 80,5 % in the microprobe analysis of the anhydrite inclusion in a quartz crystal could indicate that there is water present and that the inclusion therefore can be gypsum (Jaroslaw Majka, personal communication May 4, 2017). The birefringence is though consistent with anhydrite 0,040-0,045, not gypsum 0,009-0,010 (webmineral.com). The analysed CaO concentration is too high and SO₃ too low to match gypsum. The CaO value match that of known anhydrite but the SO₃ value is too low to match and by normalization for anhydrite the CaO value gets too high and the SO₃ is still too low. A possible explanation might be that the inclusion was gypsum at enclosure in the quartz crystal and then got dehydrated into anhydrite at burial and the water remained together with excess CaO. A table of the microprobe analyse values together with known values for anhydrite and gypsum is presented in table 5.

Wt%	inclusion		Known anhydrite	Known gypsum
	Inclusion microprobe	Normalized for anhydrite		
CaO	40,91	51,38	41,19	32,57
NiO	0,0885			
FeO	0,6269			
MnO	0,0041			
Cr ₂ O ₃	0,0025			
V ₂ O ₃	0,0053			
F	0,116			
SO ₃	38,72	48,62	58,81	46,50
H ₂ O	Not analysed			20,93
Total:	80,5065		100	100

Table 5. Microprobe analysis of inclusion in a quartz crystal in sample 17-BH-PAS-08.

In the same unit as the first samples collected as possible anhydrite pseudomorphs there are two lighter coloured layers with an erosion surface on top not marked in the profile, see figure 22 a. The layer marked as breccia in the stratigraphic profile in section C on top of one of the dolostone units have elongate pebbles, see figure 22 b. These elongate shapes do also resemble ghost gypsum. In figure 22 a few of the elongate clasts (marked by a red-dotted line) have a shape very similar to swallow-tail twinned gypsum.

With several other layers confirmed and/or interpreted as replaced gypsum beds in the stratigraphic profile; there is a possibility that these beds can be replaced gypsum beds too.



Figure 21 a). Elongate shapes in cut surfaces of sample 17-BH-PAS-09. b) Lenticular gypsum shape is applicable on a cut surface of sample 17-BH-PAS-08.

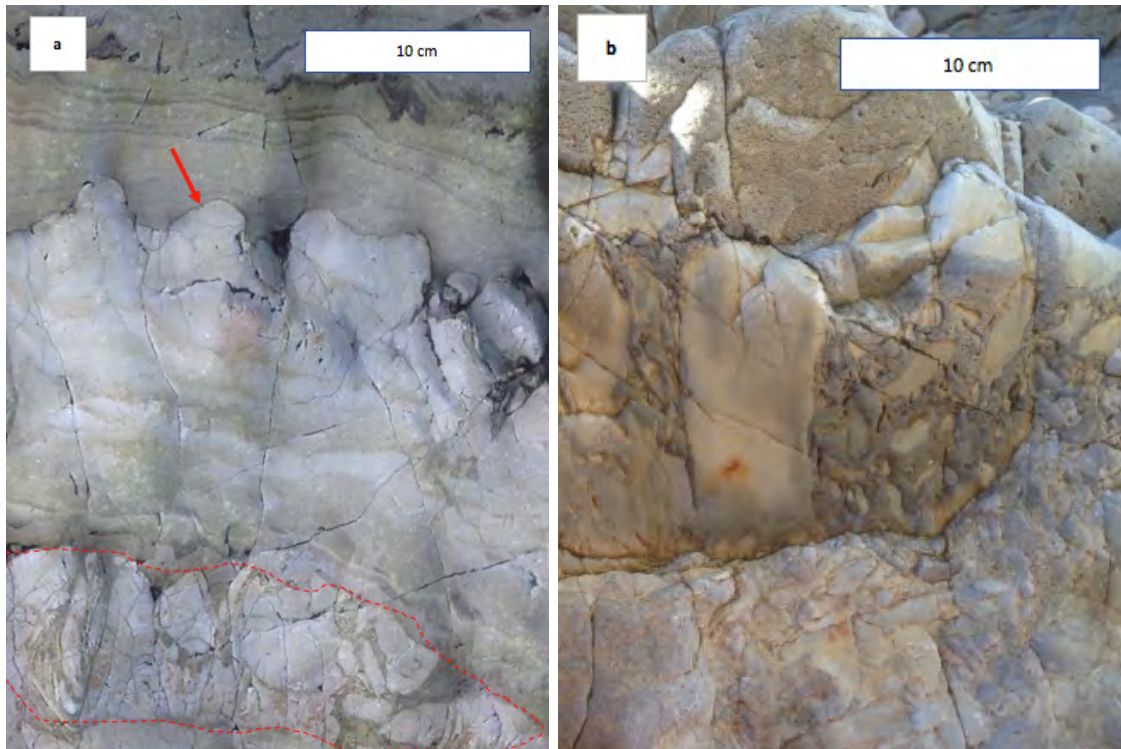


Figure 22 a). Erosion surface in a “wave-polished dolostone with dark thin mud/dolostone interbedding”- unit. The red arrow point at the upper erosion surface. The lower erosion surface have elongate clasts and is marked with a dotted red line. **b)** “Breccia” with elongate pebbles.

The pseudomorphs in the organic meta-mudstone will be referred to as type 3 pseudomorphs. These pseudomorphs do not have the abundant microcrystalline quartz edges/areas seen in type 1 and 2 pseudomorphs. Many quartz grains in type 3 pseudomorphs are instead elongated in the direction of grain alignment of the surrounding matrix (fig. 23, right).

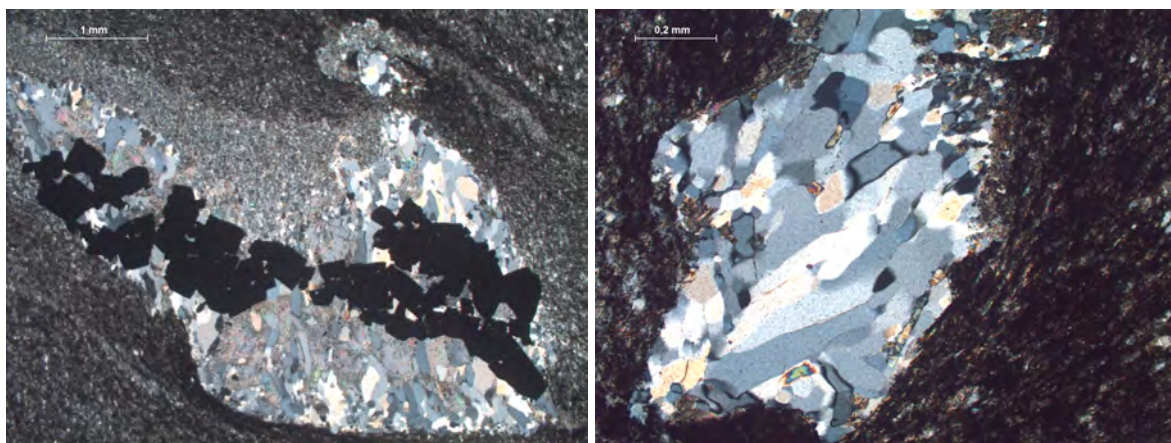


Figure 23. Pyrite clustered along the length of the pseudomorph (left). Elongate quartz grains with angular inclusions with a birefringence consistent with anhydrite (right). Both pseudomorphs are from sample 17-CO-PAS-03 collected by Christina Ohrazda.

The pyrite has the largest grainsize and appears in clusters in type 3 pseudomorphs (fig. 23, left). In type 1 and 2 pseudomorphs the pyrite is fine-grained and spread out; preferably in the outer regions of the pseudomorphs. The organic meta-mudstone where sample 17-BH-PAS-01 was collected from is very dark. It also had the highest Si-, Al- and K-content of the

handheld XRF-analysed samples which indicate high input of continental weathering products. The hand-held XRF-results from the first dolostone unit and the meta-mudstone is compared in table 6.

Sample (area)	Mg (wt%)	Al (wt%)	Si (wt%)	K (wt%)	Ca (wt%)	Fe (wt%)
17-BH-PAS-01 (dark matrix)		5,71	21,12	5,30	3,32	2,95
17-BH-PAS-08 (dolostone matrix)	4,01	2,58	13,37	2,42	12,47	2,23

Table 6. Hand-held XRF-values of the dolostone matrix and meta-mudstone matrix.

FeS is giving a black colouration of sediment (Schlesinger,1997). Nowhere in the units above this dark colour is present; but instead pyrite laminae. This might be explained by the balance between weathering products and sulphate reducing bacteria (SRB).

A possible chain of events leading to the type 3 pseudomorphs could be as follows:

1. The input of new sulphate and iron oxides from weathering after glaciation might during this time have been higher than the rate of bacterial sulphate reduction.
2. All available H₂S produced by the sulphate reducers could have reacted with Fe²⁺ produced by iron reducers from iron oxides; leaving FeS in the sediment without further available H₂S to form pyrite. With abundant sulphate in the pore-waters in the SRB-levels of a mat or within sediment, the SRB will not dissolve calcium sulphate.
3. Some of the gypsum that got formed at the sediment surface might have been dissolved by less saline water that brought in the wash-over sands forming the thin/lenticular sand/dolostone interbedding. Sand replaced the gypsum shapes where gypsum got dissolved.
4. The remaining gypsum got buried and dehydrated without much early replacement of silica via SRB activity. Some of the resulting anhydrite got enclosed by recrystallizing silica sand at depth under pressure resulting in elongate quartz.
5. The remaining anhydrite that did not get included in quartz dissolved during metamorphism and the sulphate got thermochemically reduced and reacted with the nearby available FeS and formed the pyrite clusters we now see in the pseudomorphs. Thermochemical sulfate reduction at depth can leave hydrocarbon inclusions (Warren, 2016). The SEM-analysed inclusions in sample 17-BH-PAS-01 that were not calcium sulphate had more carbon than fitting the available calcium for calcite that might be such hydrocarbon inclusions.

5.3 Sedimentary structures and microfossils

Polygonal structures connecting shrinkage cracks are described by Fairchild (1980a) as commonly occurring in the Bonahaven Dolomite Formation. The description of microbially induced sedimentary structures in the introduction of this study and the images of polygonal structures in drying microbial mats in the same section suggest a microbial mat origin of the polygonal patterns. The organic network in sample 17-BH-PAS-05 could provide proof of this if it is confirmed as a microbial mat fossil.

In this study, the shrinkage cracks are described as “deformed crack-fills” where dolo-sand is filling cracks in organic meta-mudstone. The features described as “deformed laminae at angle to bedding” in this study (fig. 24) can be seen on both fresh and weathered surfaces that have the same appearance as the suspected microbial mat surface. The dark laminae/flakes

could be the remnants of cyanobacterial migration upwards when sediment covering blocks sunlight as described in section 1.3.1 (Noffke et al., 2013). Fairchild (1980a) also describes irregular-topped dolostones with flake-pockets. Flakes and thin brown layers stand out in relief where the adjacent carbonate has weathered more (fig. 25). These have the same appearance as the suspected microbial-mat surface of sample 17-BH-PAS-05. The wave-eroded surface (fig. 24) is by correlation to the stromatolite mound outcrop the same lithology as the chemically weathered surface in figure 25 and 26 (left). The dark thin interbedded mud/dolostone is analogous to the brown surfaces in figure 26 which shows the outcrop (left) and a dolostone with dark interbedded mud/dolostone from section C (right).

Other features described by Tanner (1998) includes mud-curls, mudstone chips and up-bent edges at shrinkage cracks. All these features and the very abundant layers of sedimentary pyrite resemble microbial induced sedimentary structures as described in section 1.2.2. The increased preservation potential of sedimentary structures from microbial mats by up to 12 times (Noffke et al., 2013) could explain why so many sedimentary structures are so well preserved in the Bonahaven Dolomite Formation despite the greenschist facies metamorphism.

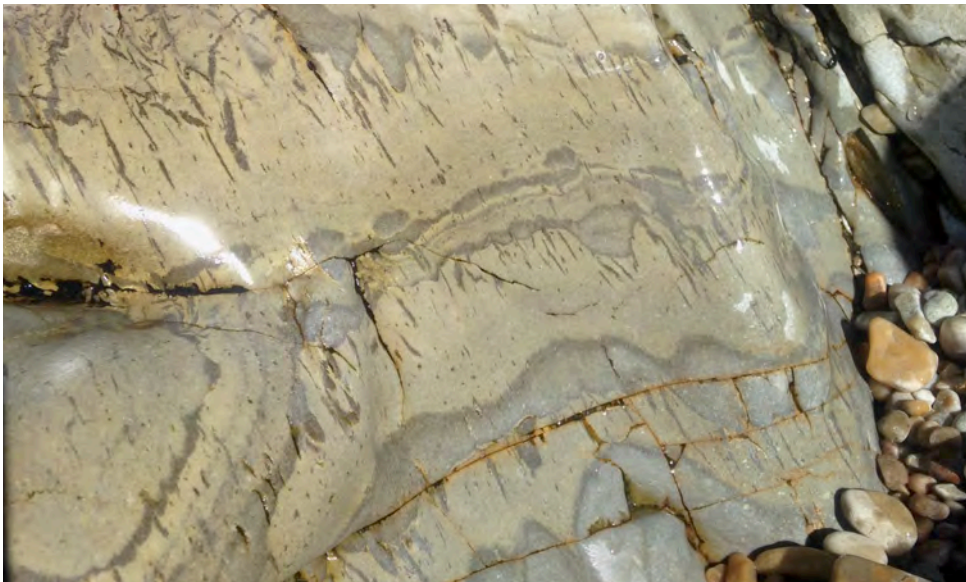


Figure 24. Dolostone with dark thin mud/dolostone interbedding and “deformed laminae at angle to bedding” and “mudflakes”.



Figure 25. Mud-flake pockets seen from above (left) and a mud-curl (right) found at the stromatolite mound outcrop.

The interpretation of the polygonal pattern of cracks by Tanner (1998) is that seismicity could have triggered the cracking and creating the pattern. Former interpretations included desiccation-cracks, “worm-casts”, frost-wedging, syneresis (shrinking of sediment under water but before burial) and aerial exposure of algal mats were all eliminated from diagnostic consideration in Tanner’s work (Tanner, 1998). The algal mat interpretation was discarded by Tanner because he could not see any evidence of desiccated algal mats “either in hand specimen or thin section” (Tanner, 1998, p.83).



Figure 26. The stromatolite mound outcrop (left). Measuring stick is 2 m. Red arrows point at yellow dolostone beds with brown thin layers standing out in relief, analogous to the lithology described as dolostone with dark mud/dolostone interbedding in this study (right). The round bump in the lower part of the left image is the stromatolite mound.

Another way of crack-fills to form is when lenticular gypsum grow and at a later stage gets dissolved during a period of less saline water inflow (Warren, 2016). Figure 27 show a possible chain of events leaving crack-fills after former gypsum crystals. The figure is reworked and modified after a figure by Warren (2016). The case described by Warren include a period of drying out and covered by sand subaerial; though this scenario might as well happen without a subaerial event since calcium sulphate can be dissolved when fresher water fills the basin (Abrantes et al., 2016). Inflow of wash-over sands as suggested by Fairchild (1991a) in the meta-mudstone units would bring in fresh water which could potentially dissolve the gypsum; leaving v-shaped cracks that got subsequently filled with the incoming sand.

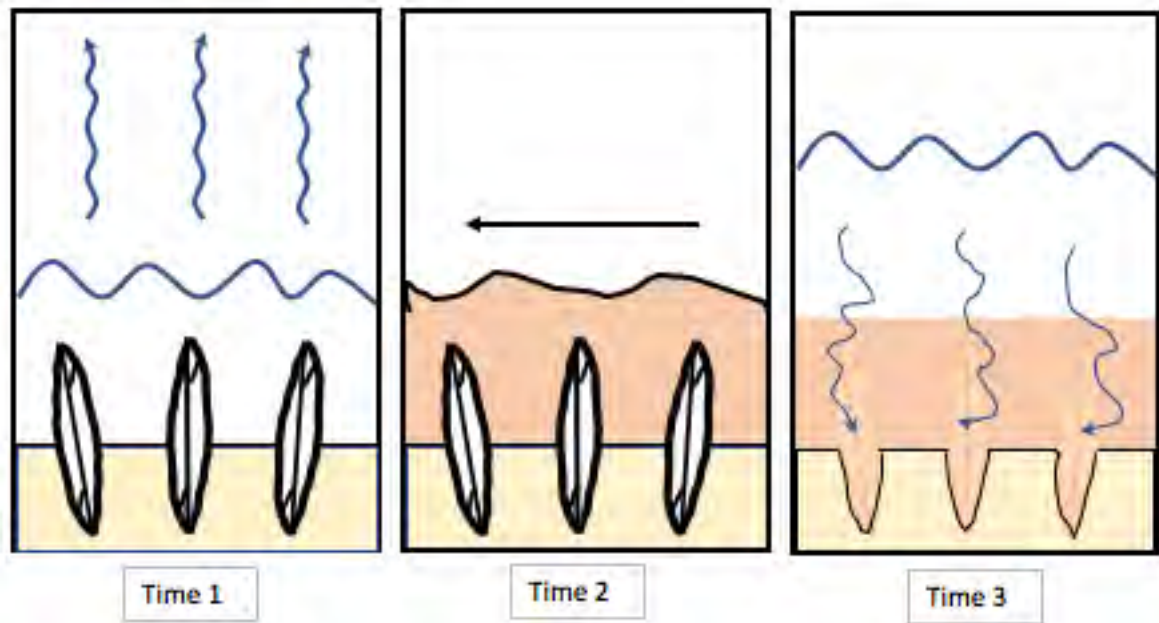


Figure 27. Figure modified after figure in Warren (2016). Time 1 represents evaporation and forming of gypsum in the sediment surface. Time 2 represents covering of the gypsum by sand (subaerial in Warren's description). Time 3 represents filling of less saline water in the basin, percolating through the sand while reworking it by wave-motion and dissolving the gypsum, leaving a sand-filled crack.

There are certain criteria to follow to find out if a suspected microfossil is indeed a microfossil (Javaux & Benzerara, 2009). The rock unit in question must have had suitable conditions for life and microfossils must be enclosed within the minerals or between grains before cementation of the rock (Javaux & Benzerara, 2009). Sediments are in most cases suitable environments for life (Javaux & Benzerara, 2009). To ensure that the microfossils are syngenetic and not of later origin; Raman spectroscopy can be used to compare with known peak values of temperature and pressure in the host rock (Javaux & Benzerara, 2009). The morphology can be compared to known biologic morphologies to make sure the microstructure is not abiotic (Javaux & Benzerara, 2009). Polygonal networks are one example of biologic microstructure (Javaux & Benzerara, 2009). Folding and flattening can be indicative of flexibility of cell walls and orientation and distribution can be indicative of mobility and interaction with the environment (Javaux & Benzerara, 2009). A brown-black colour is characteristic for organic-walled microfossils (Javaux & Benzerara, 2009).

The network structure in sample 17-BH-PAS-05 has a high carbon content, a polygonal structured network and have a brown-black colour. Elongation of network openings along crack edges are present; which could represent the contraction of the drying network causing it to crack. The surface of the sample is tufty and folded. An orientation perpendicular to bedding of filaments of the network is present. The high phosphor content of the analysed network is also an indication of organic material and the cracks with oxidized surface indicate that the organic network is not of modern origin (Magnus Ivarsson, personal communication, May 15th, 2017). The structure of the network is similar to the cellular colony structures formed by entophysalis or similar cyanobacteria (Therese Sallstedt, personal communication, May 15th, 2017). A SEM image of a entophysalis network where the bacteria is still present is presented in figure 29 for comparison (Kazmierczak et al., 2012). All these features indicate a biologic origin. The organic network can thereby be considered as having a biogenetic origin and is interpreted a microbial mat fossil which is agreed upon by Magnus Ivarsson and

Therese Sallstedt at Swedish Museum of Natural History (personal communication, May 15th, 2017). The microbial mat fossil is syngenetic with narrow calcite veins, which indicate a late stage depositional syngeneity (Magnus Ivarsson, personal communication, May 15th, 2017). There are at least three more biofilm generations within the thin section which approve with a syngenetic origin. The syngeneity approves that the microbial mat was formed at deposition of the Bonahaven Dolomite Formation, not later.

A secondary electronic image showing two fossil microbial mat segments that have grown upwards from the horizontal mat surface is presented in figure 28 a. Cyanobacteria migrate in a vertical direction to reach the light after being covered by sediment (Noffke et al., 2013). The sediment cover is now eroded away from the surface in the sample. These vertical growths and the description of vertical migration of cyanobacteria to reach sunlight when covered by sediment are supportive of an interpretation of the “mud-flake” pockets (fig 25) and deformed laminae at angle to bedding as vertical growing segments of microbial mats.

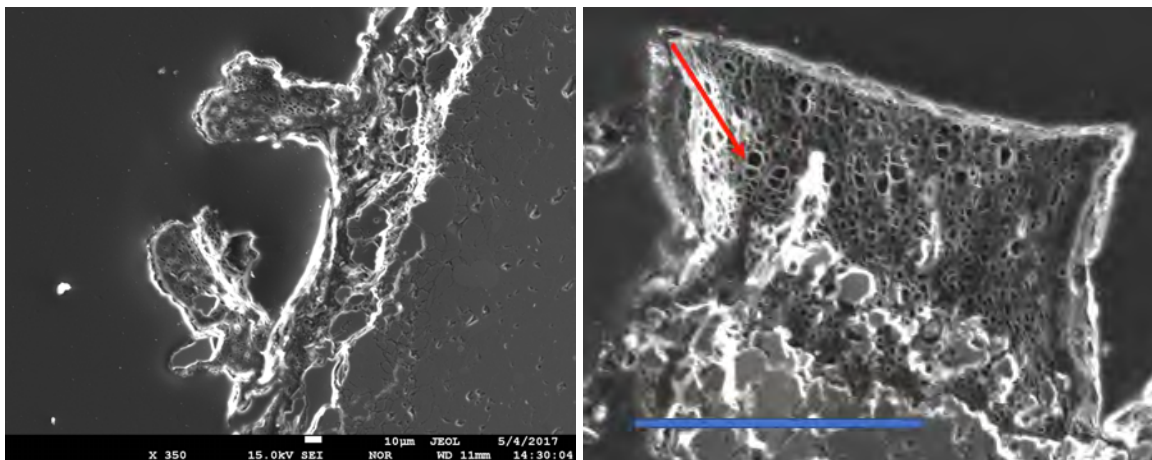


Figure 28 a). Secondary electronic image (SEI) of a part of the microbial mat microfossil where two segments grow with an upward orientation. **b)** Close-up of an SEI of the microbial mat fossil. Scalebar 100 μm . Red arrow is pointing at a split cell structure (Therese Sallstedt, personal communication, May 15th, 2017). Original images taken by Iwona Klonowska, Uppsala University.

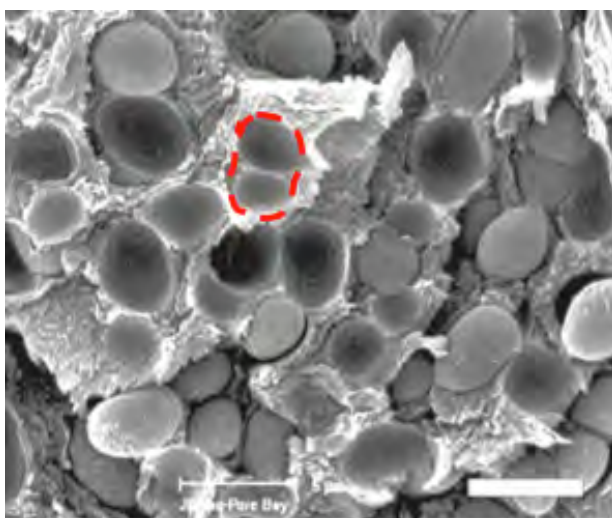


Figure 29. SEM image of modern colonial coccoidal cyanobacteria (*Entophysalis* sp.) from Lake Van, Turkey (Kazmierczak et al., 2012). A split cell is outlined with red dotted line. Scalebar is 5 μm . This split cell is about half the size of the split cell pattern in figure 28 b, though there are abundant smaller holes in the network of the sample and there are various sizes of the cyanobacteria in this SEM-image.

Sample 17-BH-LL-01 from the Lossit Limestone contains several dark organic-looking laminae. By comparing with photos from thin-sections in Noffke et al. (2013) the dark laminae look like typical microbial mat network laminae. The laminae are clearly syngenetic (Magnus Ivarsson, personal communication, May 15th, 2017). If these laminae would also be microbial mat remnants; it would be supportive of the Cryogenian glaciation interpretation that will be discussed in section 6. A close-up microphotograph of one of the laminae is presented in figure 30 a and images of typical microbial mat laminae is presented in figure 30 b (Noffke et al., 2013)

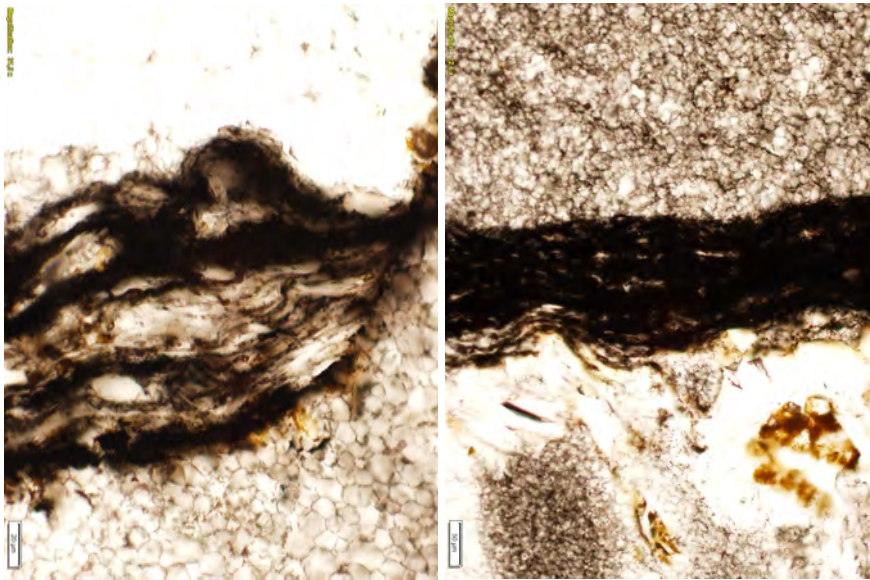


Figure 30 a. Microphotographs of organic looking laminae in sample 17-BH-LL-01 (microphotographs by Magnus Ivarsson, Swedish Museum of Natural History). Left scalebar 20 µm and left scalebar 50 µm.

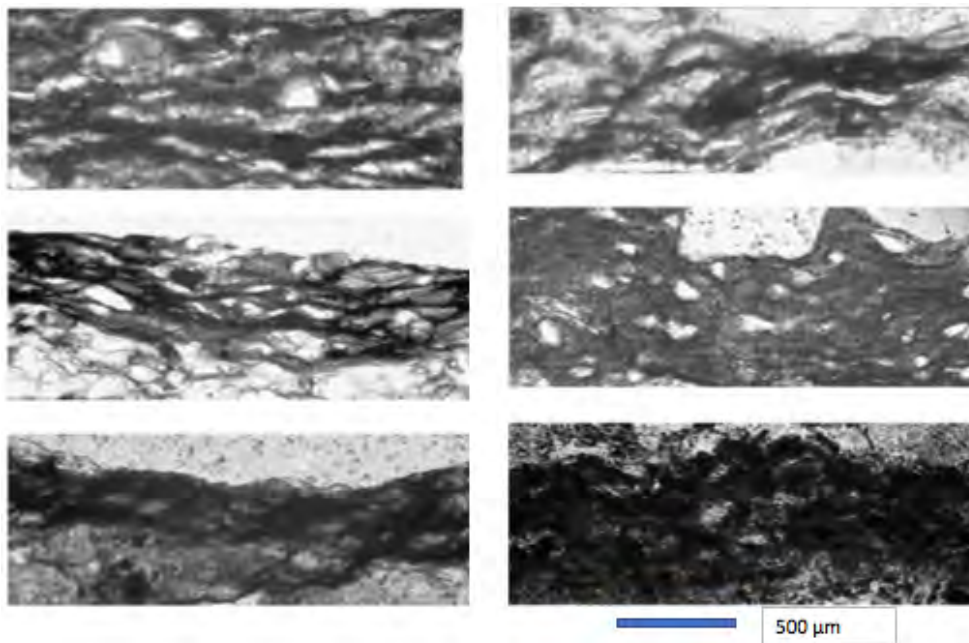


Figure 30 b. Network forming laminae typical for microbial mats in thin section (Noffke et al. 2013).

5.4 Environment interpretation

The presence of gypsum and anhydrite indicate that the Bonahaven Dolomite Formation at least periodically was deposited under evaporitic conditions. The Bonahaven Dolomite Formation is characterized by dolomite. Dolomitization by brine reflux and at burial is common in carbonate evaporites (Warren, 2016) and is a potential explanation of dolomite occurrence. Pyrite is present in stratabound laminae in most lithologies of the study area and some pseudomorphs are directly on top of, under or penetrating pyrite laminae. Pyrite formation requires reduced sulphate which is found in anoxic conditions (Tziperman et al., 2011). Organic matter can be preserved in evaporitic carbonates; creating the possibility for hydrocarbons to form or provide the reductants needed for pyrite formation at diagenesis (Warren, 2016). Anoxic conditions are however required for organic material to be preserved within sediment. Calcium sulphate formation requires an oxygenated environment for SO_4 to be saturated enough for precipitation (Turner & Bekker, 2016). The surface of microbial mats is oxygenated by cyanobacteria (Dupraz et al., 2008). Anoxic conditions and sulphate reducing bacteria are found within approximately two mm below the surface of a microbial mat (Dupraz, 2008). Dolomite can be directly precipitated within microbial mats via sulphate reducing bacteria (Wright & Wasey, 2005).

Dolomite together with approximate occurrence of gypsum pseudomorphs and strata-bound pyrite thereby indicate a microbial mat mediated environment of deposition. All units described as dolostone have small white dots which could potentially match the description of the clotted macrofabric of thrombolite in section 1.2.1. The presence of a carbonaceous network laminae that fulfils several requirements for being identified as a microfossil supports this interpretation. The microcrystalline edges and the inclusions confirmed as gypsum in type 1 pseudomorphs indicate an early replacement mediated by sulphate reducing bacteria which is also supportive of a microbial mat environment. The well preserved sedimentary structures in the Bonahaven Dolomite Formation is a possible indication of microbial mat stabilisation.

The presence of gypsum indicates a shallow water environment (<10m) (Schreiber & Tabakh, 2000, Nichols, 2009, Warren, 2016) which is consistent with Fairchild's (1991a, b) descriptions of unit 4 of member 2 as a lagoonal deposit and member 3 as mainly lagoonal with occasional storm-events. The elongate pseudomorphs resembling ghost gypsum indicates a salinity level of 250-300G/L suitable for selenitic gypsum growth. Lenticular gypsum indicates high (+35°C) temperature of deposition (Warren, 2016). Water becomes denser at evaporation due to the higher salinity which make the evaporation rate slow down but cause a higher proportion of infrared sunlight to refract back into the water, increasing the internal temperature of the water body to 35-55°C (Schreiber & Tabakh, 2000). The higher internal temperature allow evaporation to occur in moderately humid regions (Schreiber & Tabakh, 2000). Wind and lower atmospheric pressure also accelerate the evaporation rate (Schreiber & Tabakh, 2000). Red coloration by halophylic bacteria that are common in salinity levels above 150g/L can cause additional temperature increases of the water with 3-6 °C (Schreiber & Tabakh, 2000). An evaporitic environment does therefor not necessarily indicate extremely arid or hot air temperature why a climate interpretation based on gypsum growth is hazardous. What can be concluded from the increased temperature effect of high salinity is that ikaite growth in a lagoonal evaporite deposit is highly unlikely.

The presence of stromatolites is associated with open-marine conditions and high wave energy and leiolites/thrombolites are associated with low wave energy and increased salinity levels (Dupraz et al. 2008). Though stromatolites can be formed by gypsum in evaporitic environments too which mean they are not confined only to open marine environment (Alwood et al., 2013). An evaporitic lagoon environment could thereby allow the presence of any microbial mat structure from high energy/normal salinity to low energy/high salinity to occur; possibly with different structures representing fluctuating inflow/evaporation in the lagoon. The presence of cracks that are filled from above could be representing either periods or parts of the lagoon being of intertidal character or warmer periods with higher evaporation leaving shallow parts of the lagoon dry or fillings of water-dissolved lenticular gypsum.

6. Wider implications of microbial effects on sedimentation

Variations in $\delta^{34}\text{S}$ between +10‰ and 30‰ is recorded in evaporites through time; representing fluctuations of the dissolved sulfate in the environment of deposition (Claypool et al., 1980). The estimated $\delta^{34}\text{S}$ values in evaporites deposited in equilibrium with the world ocean at the end of the Proterozoic range between 30 and 35‰; which are the highest values during the last 1000 Ma (Claypool et al., 1980). The unusually high $\delta^{34}\text{S}$ values could be explained by depletion of ocean SO_4^{2-} by sulfate reducing bacteria (Hurtgren et al., 2002). During glaciation periods the provision of sulfate to the ocean decrease because no chemical weathering of pyrite could occur when continents are covered by ice (Hurtgren et al., 2002). The fractionation that occurs because the bacteria incorporates the lighter ^{32}S sulfate makes the relative amount of ^{34}S in the ocean sulfate to increase (Hurtgren et al., 2002). With a shrinking pool of sulfate; the decrease in available ^{32}S makes the fractionation smaller and smaller with a resulting higher and higher ^{34}S content (Hurtgren et al., 2002).

In the context of the explanation of the high sulfur isotope values by Hurtgren et al. (2002); the initial snowball-Earth hypothesis where the low $\delta^{13}\text{C}$ values prior to glaciation events are suggested to be caused by a collapse of biologic production is contradicted. In a scenario where production by photosynthesis would cease and the sulfate reduction process would proceed; CO_2 levels would rise and prevent a snow-ball earth (Tziperman et al., 2011). Cyanobacteria can live in any temperature down to at least -20°C (Warren, 2016); which make a scenario where biologic production collapse is caused by low temperature unlikely.

A possible chain of events triggering glaciations but preventing a full snowball-Earth scenario is presented in figure 31. This is a scenario that include the effects of rifting on microbial mat habitats and the potential effects of microbial mats on climate change. The scenario is similar to the biological cause for glaciation presented by Tziperman et al. (2011) with the difference of counting in only the microbial mat effects instead of water-column bacterial processes. The position of the land mass making up Rodinia by the Grenvillian orogeny at low latitudes promoted high chemical weathering (Tziperman et al., 2011). This provided ferric iron and sulfate to the ocean (Tziperman et al., 2011). With high amounts of sulfate and ferric iron available; the process of sulfate reduction and pyrite formation can draw down the atmospheric pCO_2 (Tziperman et al., 2011). The high rate of element cycling rivals that of modern rainforests per surface area (Dupraz & Visscher, 2005). This suggest that the potential rate of CO_2 drawdown is comparable with that of rainforests.

A drawdown of atmospheric CO_2 can lead to a colder climate; leading to glaciation periods (Tziperman et al., 2011). The up-going trend in $\delta^{13}\text{C}$ values during glaciations seen in the $\delta^{13}\text{C}$ –curve presented in figure 1 (Gaucher et al., 2009), can in this scenario be explained by a depletion in sulphate leading to decreased carbonate precipitation via sulphate reducing bacteria. The dip in $\delta^{13}\text{C}$ values in the end of glaciation periods would reflect the renewal of a sulphate pool by increased input from weathering when the melting of ice exposes rock to the atmosphere.

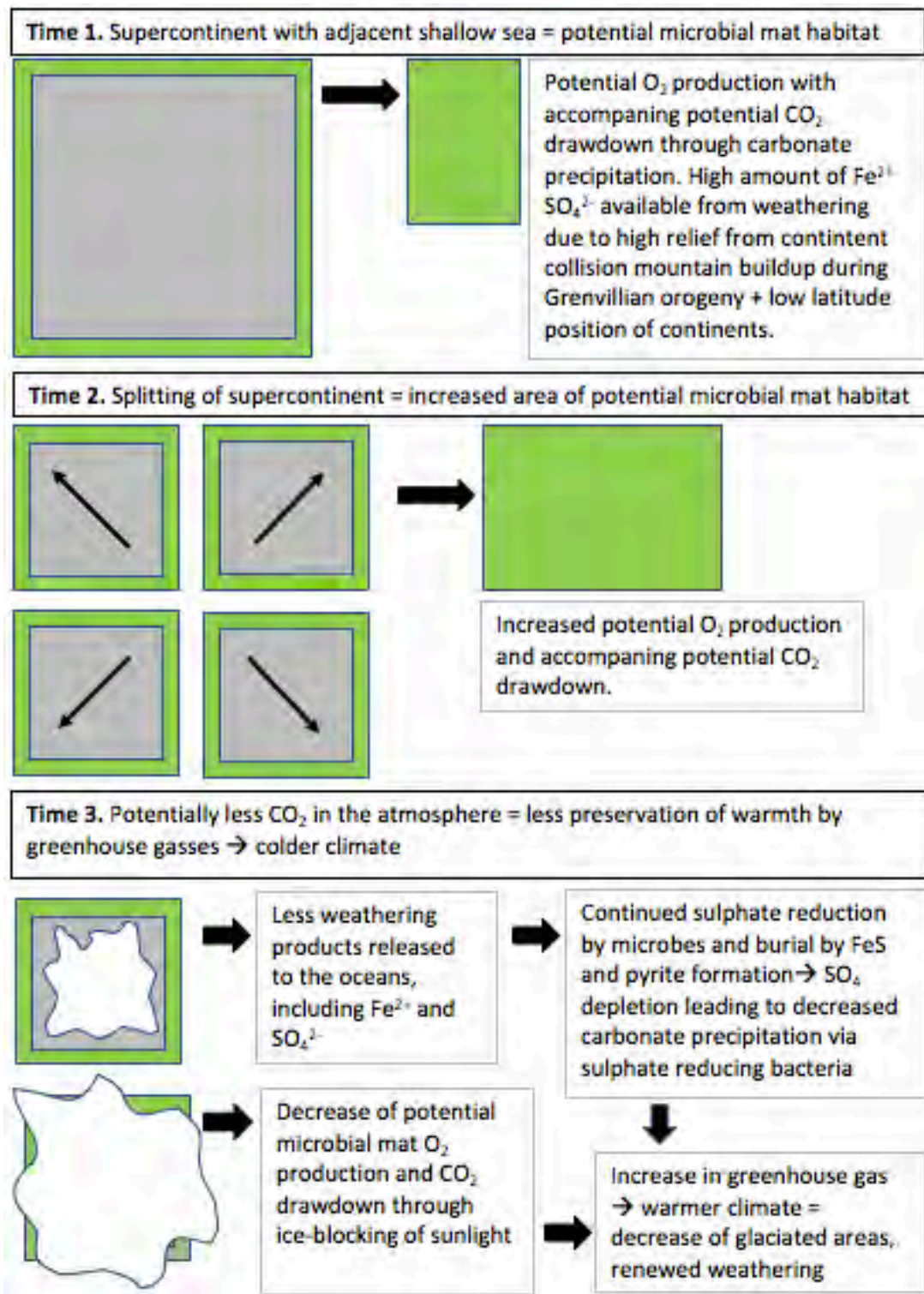


Figure 31. A possible chain of events based on microbial mat activity triggering glaciations but preventing a full snowball-Earth scenario.

Conclusions

Inclusions that are present in all types of sampled pseudomorphs including the suspected ikaite pseudomorphs are confirmed to be anhydrite in sample 17-BH-PAS-08 and 15-NI-01. The elongate shape of type 2 pseudomorphs resembles “ghost gypsum” and type 1 pseudomorphs have lenticular gypsum shape. Type 3 pseudomorphs are found together with and sometimes within frequently occurring sand-filled cracks. The wider v-shaped cracks are suggested to be traces of lenticular gypsum partly or completely dissolved by inflowing less saline seawater. Gypsum precursors are suggested for all anhydrite pseudomorphs. At least periods of the deposition of the Bonahaven Dolomite Formation can thereby be concluded to have been evaporitic sequence in a shallow (<10m) lagoon environment suiting gypsum formation. Type 1 pseudomorphs and the edges of type 2 pseudomorphs are suggested to have been replaced by microcrystalline quartz and pyrite via sulphate reducing bacteria in an early stage of burial before dehydration into anhydrite. Type 2 pseudomorphs are suggested to have been dehydrated into anhydrite at an early stage of burial and shrinkage and pressure deformed the original selenitic shapes leaving ghost gypsum that were replaced by calcite, quartz and less amounts of barite at a later stage. Type 3 pseudomorphs are suggested to have been partly dissolved by less saline water, dehydrated at burial and then replaced during later stage burial/metamorphism. The presence of stratigraphically bound pyrite layers and anhydrite pseudomorphs, well preserved sedimentary structures and confirmed microbial mat microfossils are together interpreted as indicators of a microbial mat environment of formation for the studied sequence of the Bonahaven Dolomite Formation.

Acknowledgements

I would like to thank following people: Alasdair Skelton for endless patience and being a great teacher, Elin Tollefsen for all help with the project and advice of future studies, David Webster for help with fault correlation and good research advices, Christina Ohrazda for great field-work company and exchange of thoughts and samples, Linda Löwhagen for company and advice of future studies, Dan Zetterberg for rock-cutting and thin-section administration, Curt Broman for assistance at the microscope, Marianne Ahlbom for SEM analysis, Iwona Klonowska and Jaroslaw Majka for microprobe analysis, Magnus Ivarsson for fossil advice, Therese Sallstedt for colonial cell advice, Otto Hermelin for making the front-page, Volker Brüchert for microbial mat advice, Jenny Söderlindh for communication, company, support and accommodation during the laboratory study in Stockholm, Evelina Rann for help at the microscope camera, company during microscopy and accommodation, Ting Fung Chong for pointing out the possible anhydrite pseudomorphs on the field coarse on Islay, Paula Howard for communication and my family for endless support.

References

- Abrantes, F. R., Nogueira, A. C., & Soares, J. L., 2016, Permian paleogeography of west-central Pangea: Reconstruction using sabkha-type gypsum-bearing deposits of Parnaíba Basin, Northern Brazil. *Sedimentary Geology*, 341, 175-188.
- Allwood, A. C., Burch, I. W., Rouchy, J. M., & Coleman, M., 2013, Morphological biosignatures in gypsum: Diverse formation processes of Messinian (~ 6.0 Ma) gypsum stromatolites. *Astrobiology*, 13(9), 870-886.
- Arnaud, E., Eyles, C.H., 2006, Neoproterozoic environmental change recorded in the Port Askaig Formation, Scotland: Climatic vs tectonic controls, *Sedimentary Geology* 183, pp. 99-124
- Bischoff, J. L., Fitzpatrick, J. A., Rosenbauer, R. J., 1993, The Solubility and Stabilization of Ikaite ($\text{CaCO}_3 \cdot 6\text{H}_2\text{O}$) from 0° to 25° C: Environmental and Paleoclimatic Implications for Thinolite Tufa, *The Journal of Geology*, 101(1), 21-33.
- Brady, A. L., Slater, G. F., Omelon, C. R., Southam, G., Druschel, G., Andersen, D. T., Hawes, I., Laval, B., Lim, D. S. S., 2010, Photosynthetic isotope biosignatures in laminated micro-stromatolitic and non-laminated nodules associated with modern, freshwater microbialites in Pavilion Lake, BC, *Chemical Geology*, 274(1), 56-67.
- Campbell, K. A., 2006, Hydrocarbon seep and hydrothermal vent paleoenvironments and paleontology: past developments and future research directions. *Palaeogeography, Palaeoclimatology, Palaeoecology*, 232(2), 362-407.
- Clarkson, E.N.K., 1998, *Invertebrate palaeontology and evolution*, fourth edition, Blackwell publishing p. 57-59
- Claypool, G.H., Holser, W.T., Kaplan, I.R., Sakai, H., Zak, I., 1980, The age curves of sulfur and oxygen isotopes in marine sulfate and their mutual interpretation, *Chemical Geology*, 28: 199-260
- Dempster, T., Jess, S.A., 2015, Ikaite pseudomorphs in Neoproterozoic Dalradian slates record Earth's coldest metamorphism, *Journal of the Geological Society*, Vol. 172 pp.459-464
- Dupraz, C., Reid, R.P., Braissant, O., Decho, A.W., Norman, R.S., Visscher, P.T., 2008, Processes of carbonate precipitation in modern microbial mats, *Earth-Science Reviews* 96 (2009) 141-162
- Dupraz, C., & Visscher, P. T., 2005, Microbial lithification in marine stromatolites and hypersaline mats, *Trends in microbiology*, 13(9), 429-438.
- Ehlers, E. G., Blatt, H., 1982, *Petrology: Igneous, sedimentary and metamorphic*, first edition, W.H. Freeman and Company, 472-475 p.
- Fairchild, I. J., 1980a, Sedimentation and origin of a Late Precambrian 'Dolomite' from Scotland, *Journal of Sedimentary Petrology*, 1980, 50 (2):423-446
- Fairchild, I. J., 1980b, Stages in a Precambrian dolomitization, Scotland: cementing versus replacement textures. *Sedimentology*, 27(6), 631-650.
-

-
- Fairchild, I. J., 1991a, Itinerary II: Topmost Islay Limestone (Appni group), Port Askaig and Bonahaven Formations (Argyll Group), Port Askaig area, Islay, in LISTER, C.J. (ed.): The late Precambrian Geology of the Scottish Highlands and Islands, Geologists' Association Guides, 44, pp. 33-41
- Fairchild, I. J., 1991b, Itinerary III: Bonahaven Formation (Argyll Group), North coast of Islay, *Ibid.* pp. 42-52
- Fairchild, I.J., Bonnard, P., Davies, T., Fleming, E.J., Grassineau, N., Halverson, G.P., Hambrey, M.J., McMillan, E.M., McKay, E., Parkinson, I.J., Stevenson, C.T.E., 2016, The Late Cryogenian Warm Interval, NE Svalbard: Chemostratigraphy and genesis, *Precambrian Research*, volume 281, 128-154
- Fairchild, I. J., & Kennedy, M. J., 2007, Neoproterozoic glaciation in the Earth System. *Journal of the Geological Society*, 164(5), 895-921.
- Gaucher, C., Sial, A.N., Halverson, G.P., Frimmel, H.E., 2009, The Neoproterozoic and Cambrian: a time of upheavals, extremes, and innovations. In: Gaucher, C., Sial, A.N., Halverson, G.P., Frimmel, H.E. (Eds): *Neoproterozoic-Cambrian Tectonics, Global Change and Evolution: a focus on southwestern Gondwana*. *Developments in Precambrian Geology*, 16, Elsevier, pp. 3-11.
- Google Earth (2017-05-03)
- Hoffman, P.F., Kaufman, A. J., Halverson, G.P., Schrag, D.P., 1998, A Neoproterozoic Snowball Earth, *Science* vol. 281, Issue 5381, pp.1342-1346
- Huggett, J. M., Schultz, B. P., Shearman, D. J., & Smith, A. J. (2005). The petrology of ikaite pseudomorphs and their diagenesis. *Proceedings of the Geologists' Association*, 116(3-4), 207-220.
- Hurtgen, M. T., Arthur, M. A., Suits, N. S., & Kaufman, A. J., 2002, The sulfur isotopic composition of Neoproterozoic seawater sulfate: implications for a snowball Earth?, *Earth and Planetary Science Letters*, 203(1), 413-429.
- Ivarsson, M., 2006, Advantages of doubly polished thin sections for the study of microfossils in volcanic rock. *Geochemical transactions*, 7(1), 5.
- Javaux, E. J., & Benzerara, K., 2009, Microfossils. *Comptes Rendus Palevol*, 8(7), 605-615.
- Jiang, G., Kennedy, M.J., Christie-Blick, N., 2003. Stable isotopic evidence for methane seeps in Neoproterozoic postglacial cap carbonates. *Nature* 426, 822–826.
- Kasprzyk, A., 2003, Sedimentological and diagenetic patterns of anhydrite deposits in the Badenian evaporite basin of the Carpathian Foredeep, southern Poland. *Sedimentary Geology*, 158(3), 167-194.
- Kazmierczak, J., Kremer, B., & Racki, G., 2012, Late Devonian marine anoxia challenged by benthic cyanobacterial mats. *Geobiology*, 10(5), 371-383.
- Knoll, A.H, 2000, Learning to tell Neoproterozoic time, *Precambrian research* 100, 3-20
- Lan, Z-W., Chen, Z-Q., 2012, Exceptionally preserved microbially induced sedimentary structures from the Ediacaran post-glacial successions in the Kimberley region, northwestern Australia, *Precambrian Research*, volumes 200-203, p 1-25
-

Last, F. M., Last, W. M., Fayek, M., & Halden, N. M., 2013, Occurrence and significance of a cold-water carbonate pseudomorph in microbialites from a saline lake. *Journal of paleolimnology*, 50(4), 505-517.

Li, Z. X., Bogdanova, S. V., Collins, A. S., Davidson, A., De Waele, B., Ernst, R. E., Fitzsimons, I.C.W., Fuck, R.A., Gladkochub, D.P., Jacobs, J., Karlstrom, K. E., Lu, S., Natapov, L.M., Pease, V., Pisarevsky, S.A., Thrane, K., Vernikovsky, V., 2008, Assembly, configuration, and break-up history of Rodinia: a synthesis, *Precambrian research*, 160 (1), 179-210.

www.mindat.org/min-1784.html (2017-05-15)

Moore, T. S., Murray, R. W., Kurtz, A. C., & Schrag, D. P., 2004, Anaerobic methane oxidation and the formation of dolomite. *Earth and Planetary Science Letters*, 229(1), 141-154.

Nichols, G., 2009, *Sedimentology and stratigraphy*, second edition, John Wiley & Sons Ltd, West Sussex, UK, ISBN 978-1-4051-3592-4, 36-37 p.

Noffke, N., Christian, D., Wacey, D., Hazen, R.M., 2013, Microbially Induced Sedimentary Structures Recording an Ancient Ecosystem in the ca. 3.48 Billion-Year-Old Dresser Formation, Pilbara, Western Australia, *Astrobiology*, volume 13, number 12, doi:10.1089/ast.2013.1030

Prave, A. R., Fallick, A. E., Thomas, C. W., Graham, C. M., 2009, A composite C-isotope profile for the Neoproterozoic Dalradian Supergroup of Scotland and Ireland, *Journal of the Geological Society*, London, Vol. 166, pp. 845-857

Rooney, A. D., Strauss, J. V., Brandon, A. D., & Macdonald, F. A., 2015, A Cryogenian chronology: Two long-lasting synchronous Neoproterozoic glaciations. *Geology*, 43(5), 459-462.

Schlesinger, W.H., 1997, *Biogeochemistry – an analysis of global change*, second edition, Academic press, ISBN-13: 978-0-12-625155-5, p. 235

Shearman, D. J., & Smith, A. J., 1985, Ikaite, the parent mineral of jarrowite-type pseudomorphs. *Proceedings of the Geologists' Association*, 96(4), 305-314.

Schreiber, B. C., & Tabakh, M. E., 2000, Deposition and early alteration of evaporites. *Sedimentology*, 47(s1), 215-238.

Skelton, A., Lewerentz, A., Kleine, B., Webster, D., Pitcairn, I., 2015, Structural Channeling of Metamorphic Fluid on Islay, Scotland: Implications for Paleoclimatic Reconstruction, *Journal of Petrology*, vol. 56, No. 11, 2145-2172

Swainson, I. P., & Hammond, R. P. (2001). Ikaite, CaCO₃· 6H₂O: Cold comfort for glendonites as paleothermometers. *American Mineralogist*, 86(11-12), 1530-1533.

Tanner, P. W. G., 1998, Interstratal dewatering origin for polygonal patterns of sand-filled cracks: a case study from late Proterozoic metasediments of Islay, Scotland. *Sedimentology*, 45, 71-89.

Turner, E. C., Bekker, A., 2016, Thick sulfate evaporite accumulations marking a mid-Neoproterozoic oxygenation event (Ten Stone Formation, Northwest Territories, Canada). *Geological Society of America Bulletin*, 128(1-2), 203-222.

Tziperman, E., Halevy, I., Johnston, D. T., Knoll, A. H., & Schrag, D. P., 2011, Biologically induced initiation of Neoproterozoic snowball-Earth events. *Proceedings of the National academy of Sciences*, 108(37), 15091-15096.

[Webmineal.com/data/Anhydrite.shtml#.WRnMb4GezYV](#) (2027-05-15)

[Webmineral.com/data/Gypsum.shtml#.WRiXKIgezYU](#) (2017-05-15)

Warren, J. K., 2016, *Evaporites – A geological compendium*, second edition, Springer International Publishing Switzerland, ISBN 978-3-319-13512-0 (eBook), doi 10.1007/978-3-319-13512-0, p 41-44, 60-62, 69-, 716-722

Webster, D., Anderton, R., Skelton, A., 2015, *A guide to the Geology of Islay – An introduction to Islay's geological past with 12 illustrative walking excursions*, Ringwood Publishing, Glasgow, ISBN 978-1-901514-16-2, 24-27 p.

Wright, D. T., & Wacey, D., 2005, Precipitation of dolomite using sulphate-reducing bacteria from the Coorong Region, South Australia: significance and implications. *Sedimentology*, 52(5), 987-1008